Quantifying salinity in heterogeneous coastal aquifers through ERT and IP: insights from laboratory and field investigations

Diep Cong-Thi[1,2], Linh Pham Dieu[1,2], David Caterina[3], Xavier De Pauw[1], Huyen Dang Thi[2], Huu Hieu Ho[2], Frédéric. Nguyen[3,4], Thomas. Hermans[1]

(1) Department of Geology, Ghent University, 9000-Gent, Belgium.

(2) Department of Marine Geology, Vietnam Institute of Geosciences and Mineral Resources (VIGMR), 100000 Hanoi, Vietnam.

(3) Department of Urban and Environmental Engineering, Liege University, B52- 4000 Liège, Belgium.

(4) Department of Civil Engineering, KU Leuven, 3000 Leuven, Belgium.

Corresponding author: diep.congthi@Ugent.be, Thomas.Hermans@Ugent.be

Abstract. The lithological and stratigraphical heterogeneity of coastal aquifers has a great influence on saltwater intrusion (SI). This makes it difficult to predict SI pathways and their persistence in time. In this context, electrical resistivity tomography (ERT) and induced polarization (IP) methods are receiving increasing attention regarding the discrimination between saltwater-bearing and clayey sediments. To simplify the interpretation of ERT data, it is commonly assumed that the bulk conductivity mostly depends on the conductivity of pore-filling fluids, while surface conductivity is generally disregarded in the spatial and temporal variability of the aquifers, particularly, once the aquifer is affected by the presence of saltwater. Quantifying salinities based on a simplified petrophysical relationship can lead to misinterpretation in aquifers constituted by clay-rich sediments. In this study, we rely on co-located data from drilled boreholes to formulate petrophysical relationships between bulk and fluid conductivity for clay-bearing and clay-free sediments. First, the sedimentary samples from the drilled wells were classified according to their particle size distribution and analyzed in the lab using a spectral IP in controlled salinity conditions to derive their formation factors, surface conductivity, and normalized chargeability. Second, the deduced thresholds are applied on the field to distinguish clay-bearing sediments from brackish sandy sediments. The results are validated with logging data and direct salinity measurements on water samples. We applied the approach along the Luy River catchment and found that the formation factors and surface conductivity of the different unconsolidated sedimentary classifications vary from 4.0 to 8.9 for coarse-grained sand and clay-bearing mixtures, while normalized chargeability above 1.0 $mS.m^{-1}$ indicates the presence of clay. The clay-bearing sediments are mostly distributed in discontinuous small lenses. The assumption of homogenous geological media is therefore leading to overestimating SI in the heterogeneous clay-bearing aquifers.

Keywords: aquifer, saltwater intrusion, conductivity, resistivity, induced polarization.

1. Introduction

Saltwater intrusion (SI) in coastal aquifers is one of the serious problems that numerous countries have to face, particularly countries with long coastlines (Motallebiana et al., 2019; Ketabchi and Jahangir, 2021). It has not only a significant local influence through the degradation of water resources, but it also affects the general development of a country (Insigne and Kim, 2010; Post et al., 2018). Evaluating the vulnerability of coastal aquifer systems necessitates a holistic approach encompassing natural elements combined with the inherent characteristics of aquifers, including their geological composition and structure governed by past climatic and tectonic settings (Changa et al., 2018; Werner et al., 2013; Cong-Thi et al., 2021a; Dieu et al., 2022). In addition, the anthropogenic influence, through activities such as excessive groundwater extraction is also crucial (Najib et al., 2017; Mora, et al., 2020; Nasiri et al., 2021).

In periods of high water level (transgression), the dominant deposition consists of fine-grained sediments, culminating in the development of clay-rich sedimentary strata. Conversely, during periods of sea-level decline (regression), previously deposited formations undergo modification and erosive processes. The coastal sedimentation patterns encompassing alluvial, aeolian, and lacustrine processes, depending on hydraulic conditions, typically lead to the accumulation of sedimentary sequences characterized by a broad range of grain sizes (Krumbein, 1934; Krumbein and Sloss, 1963). The succession of numerous regression-transgression cycles is the main cause for the formation of complex depositional sequences, resulting in the strong heterogeneity of many coastal aquifers (Miall, 2000; Ta et al., 2001; Nguyen et al., 2017) and a considerable impact on SI existence and characteristics.

From a hydrogeological perspective, mapping the geometry and physical properties of aquifers in a coastal setting is a difficult task and requires a large amount of data. Frequently, this task relies on previously collected geological information pertaining to lithological and stratigraphic records, but it is time-consuming and lacks reliability when the data are too sparse. To generate continuous and spatially distributed data, borehole logs can be combined with geophysical methods (Martínez et al., 2009; Baines et al., 2022). In case of contamination through SI processes, the task is even more complicated (Cong-Thi et al., 2021a).

Electrical Resistivity Tomography (ERT) is sensitive to the resistivity variations of the subsurface which depends on the pore-filling fluid and lithology. Recovering the lithological heterogeneity of coastal aquifers from ERT is a challenging task, particularly in saline conditions because low resistivity values can be attributed to either brackish-salt water or clay-rich sediments or both (Nguyen et al., 2009; Tassy et al., 2019). To estimate the salinity from the bulk resistivity distribution, the most common approach is to use Archie's law (Archie, 1942) which estimates the formation factor (F) relating the conductivity of pore-filling fluids to that of the saturated porous medium, depending itself on the porosity and tortuosity (Lyons, 2010; Schön, 2011). The role of surface conductivity related to the electrical double layer (EDL) is ignored in this model. However, the latter contributes significantly to the increased conductivity in the presence of clay (Waxman and Smits, 1968; Vinegar and Waxman, 1984; Revil and Skold, 2011; Revil et al., 2017). Although the pore fluid effect is dominant in high salinity environments, allowing mapping of saline zones with relative certainty, the surface conductivity effect prevents the identification of freshwater resources when clay is present, as they can be easily misinterpreted as brackish zones (Szalai et al., 2009; Michael et al., 2016; Cong-Thi et al., 2021a).

Induced polarization (IP) measures the ability of the subsurface to store electrical charge under the impact of an electric field (Marshall et al., 1959). Time-Domain IP (TDIP) surveys are conducted similarly to ERT surveys, by sending a current into the ground while measuring the resulting potential difference. After shutting the current off, the potential decay in the subsurface is measured in several time windows to characterize its chargeability, which is the ratio of the secondary voltage (decay) over the primary voltage of the transmitted current. Dividing the chargeability by the resistivity results in the normalized chargeability that might highlight zones with high surface conductive properties (Magnusson et al., 2010; Slater et al., 2002) such as clay-rich media. Higher normalized chargeability is expected in clay-rich sediments while coarser-grained soils including sand, gravel, and grit commonly yield lower values (Alabi et al., 2010). IP surveys have proven to be an effective tool for mapping the lithological layers of unconsolidated sediments, in particular the presence of clay (Benoit et al., 2019).

Nevertheless, the TDIP method exhibits a lower signal-to-noise ratio (SNR) than ERT, which is inherent to the measurement principle. TDIP is, therefore, more sensitive to noise and can occasionally lead to low quality dataset. This sensitivity is contingent upon diverse factors, including field conditions, measurement configurations and equipment (Dahlin et al., 2002; Dahlin et al., 2012), and might require some adapted measurement and processing strategies such as the use of non-polarizable electrodes (Dahlin et al., 2002), decoupling current and potential cables (Dahlin and Leroux, 2012), sorting measurements protocols (Kemna et al., 2012) or removing noisy decay curves from the data sets (Evrard et al., 2018). High conductivity encountered in saline conditions leads to even lower measured signals and makes the method quite challenging to apply for SI studies (Attwa et al., 2011).

To mitigate the uncertain interpretation of field-scaled phenomena and understand the underlying processes, laboratory-scaled methodologies are commonly applied (e.g., Revil et al., 2017). This strategic approach is intended to facilitate a more rigorous comparison and validation of observations and a broader understanding of certain components that exhibit minimal variation under field conditions.

Spectral induced polarization (SIP) measures the complex conductivity of the subsurface at various frequencies. SIP is considered as the optimum solution to characterize the interfacial polarization at the interface between materials and pore-filling fluids (Korošak et al, 2007; Revil and Florsch 2010; Revil and Skold, 2011), contributing to the complex conductivity of porous materials. If the dependence of the complex conductivity on the mentioned-above factors is dissected in laboratory experiments, it will help to distinguish the origin of conductive anomalies (Waxman and Smits, 1968; Vinegar and Waxman, 1984; Revil and Skold, 2011).

Recent petrophysical models have been proposed linking the complex conductivity of clayey soil to the clay content, the cation exchange capacity, and the formation factor (Revil et al., 2017). However, the direct application of laboratory-scale petrophysical relationships at the field scale ignores effects related to the geophysical inversion (Day-Lewis et al., 2005; Hermans and Irving, 2017). The recent investigation conducted by Dimech et al. (2023) explores the impact of measurement scale on the validity of volumetric water content (VWC) predictions in mine tailings using Electrical Resistivity Tomography (ERT). The study investigates five distinct experimental configurations to simultaneously monitor bulk electrical conductivity through time-lapse ERT and VWC through hydrogeological sensors placed in co-located positions. Subsequently, datasets are calibrated for petrophysical models across various scales. While the extensive validation of laboratory petrophysical relationships at the field scale has been limited (McLachlan et al., 2020), the petrophysical models from Dimech highlight that the validity observed at the laboratory scale remains globally valid at larger scales and could be applied to field data. However, the petrophysical models still show a broad variability around the best fit regression model, especially at scales showing more variability in the water content.

In a previous study, Cong-Thi et al., (2021a) qualitatively delimited the extent of saltwater intrusion in the Luy River catchment using ERT. However, in the absence of co-located data, their method was based on the identification of the response of clay in freshwater conditions. Intermediate values of resistivity could not be unequivocally interpreted as they could correspond to clay-rich or brackish water zones. The objective of this study is to develop a methodology combining laboratory and field measurements to characterize the petrophysical relationship in heterogeneous aquifers based on co-located data. The discrepancy of resistivity values controlled by the presence of clay minerals and salinity is identified using the lithological and hydrological information. Firstly, the co-located sedimentary samples are classified through particle size distribution analysis (PSD). Secondly, the petrophysical relationship for different grain-sized patterns is estimated based on spectral induced polarization (SIP). Lastly, the validity of the laboratory petrophysical relationship at the field scale is assessed by comparing ERT and TDIP data with high-resolution logs and total dissolved solids (TDS) content from water samples. The methodology is applied to better characterize the heterogeneity and salinity of the coastal aquifer of the Luy River catchment in Vietnam.

2. Study area

The Luy River catchment is located in Binh Thuan, a Southern Central province in Vietnam (Fig. 1), and is governed by a complex geological and tectonic context. Terrains on both sides of the river are quite different: low plains dominate on the left bank, while huge sand dunes are present on the opposite bank. Along the Luy River, the unconsolidated sedimentary sequences formed during both the Pleistocene and Holocene periods are discontinuously present in various thicknesses. The Pleistocene sediments were deposited during successively transgressive and regressive stages (Hoang Phuong, 1997). Our lithostratigraphic data recorded in the borehole logs shows that the Pleistocene layers have a low thickness on the left bank, while they are relatively thick on the right bank (Cong-Thi et al., 2021b). Sediments derived from marine-alluvial sources (Hoang Phương, 1997; Cong-Thi et al., 2021a) are composed of clean sand, clay, clayey sand sometimes containing grits, gravels, and small rocky fragments derived from pre-host rocks. Well-rounded quartz dominates while feldspar and other minerals (ilmenite, limonite, mica) are present as minor components in the lithological units (Cong-Thi et al., 2021b).

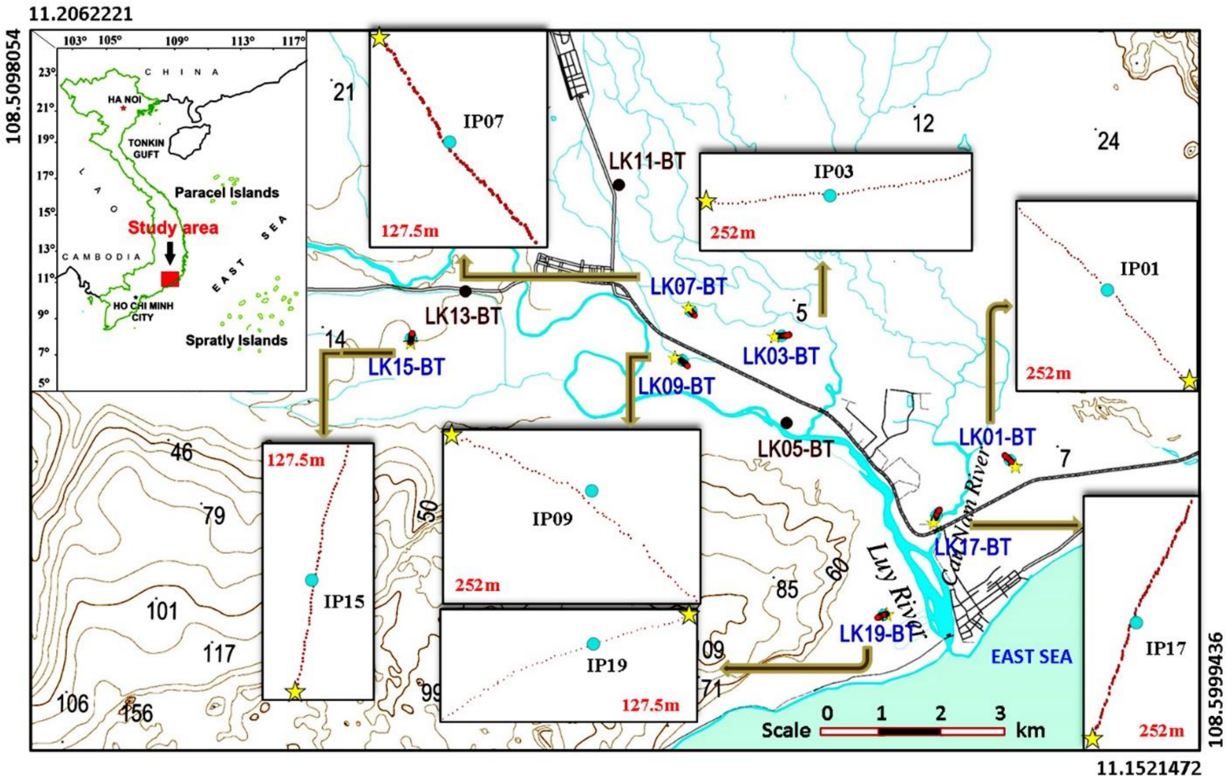

Figure 1: Location of the study site. Boreholes are indicated by brown and blue circles. Geophysical measurements coincide with the green boreholes. Yellow stars indicate the first electrode in geophysical lines whose lengths are specified in red. The analyzed unconsolidated samples were collected from these boreholes.

The Holocene sediments were dominantly accumulated through the Flandrian transgression during the Early-Middle Holocene and regression in the Middle-Late Holocene (Hoang Phuong,1997; Tran Nghi et al., 2007). The former is supported by the profile of LK07-BT and LK13-BT (Fig. 1) with the grain size decreasing gradually from clay-bearing coarser sand close to the bedrock to fine clayey sand near the surface (Cong-Thi et al., 2021b). The latter is proven by grain-sized descriptions of LK01-BT, LK17-BT, and LK19-BT. The Holocene layer with a thickness of 2 m to 20 m is characterized by alternating sedimentary layers of varying compositions such as sandy layers with interbedded clayey sand, and sandy clay layers, sometimes including fine-grained silt. The lithological composition including arkose and lithic-arkose sand was possibly connected to the sandy debris derived from the magmatic arcs, subduction complex, and eroded granitoid in the older tectonic setting (Dickinson, 1979; Miall, 2009) and complemented by deposition formed in lagoons that were forming a group of alluvial-marine transition facies (Nguyen Van Vuong, 1991; Hoang Phuong, 1997). Moreover, the local presence of multi-colored clay lenses forming locally aquitard units and containing black humus is characteristic of this period.

The transgressive and regressive cycles induced repeated sea-level changes combining depositional and erosional effects, and sedimentary discontinuity, resulting in lowstand, transgressive, and highstand systems tracts (LST, TST, HST respectively) (Tran Nghi et al., 2007). Obviously, the sea-level changes played a vital role in the variation of the sedimentary compositions and the presence of seawater in aquifers. Recent hydrogeological investigations revealed that the aquifer system is experiencing a long-term freshening trend, likely since the last water highstand, but is locally affected by salinization resulting from anthropic activities (Dieu et al., 2022). Paleo-seawater has been entrapped in the clay-rich sediments, the heterogeneous nature of sediments therefore plays a major role in the various distribution of salinity in the study area (Dieu et al., 2022).

3. Methodology

3.1. Laboratory measurement

3.1.1. SIP measurement configuration

To scrutinize the petrophysical relationships of the porous sediments, the complex electrical conductivity of various grain-sized categories is first investigated at the laboratory scale through SIP measurements. We rely on the SIP system proposed by Zimmermann et al. (2008) using the four-point measurement method represented by two electrodes for current injection and two other electrodes for potential differences (Appendix A). A polyvinyl chloride sample holder

32 cm long with a 3 cm inner diameter was employed. The potential (brass) electrodes were spaced 12.5 cm from the current electrodes, 7 cm apart (twice the inner diameter of the sample holder), and retracted from the sample to reduce polarization effects and phase errors to the resolution limit of the system (< 0.1 mrad below 1 kHz, (Zimmermann et al., 2008; Revil and Skold, 2011)). Current electrodes were inserted across the whole section perpendicular to the main axis of the sample holder. In order to further reduce phase inaccuracy, we verified that the contact impedance was smaller than the sample impedance (Zimmermann et al., 2008).

Two separate procedures are used for the clay-free and clay-bearing samples. Clean sand with natural moisture was compacted into the sample holder to obtain a homogenous density. The filled sample column was fully saturated under five different electrolytes (NaCl solution) of respective conductivity 2.59 $mS.m^{-1}$, 25.2 $mS.m^{-1}$, 392 $mS.m^{-1}$, 1793 $mS.m^{-1}$, and 5560 $mS.m^{-1}$ corresponding to deionized, fresh, slightly brackish, brackish, and saline water respectively. The three first solutions correspond to low and moderate salinity conditions while the two remaining values represent higher saline conditions. To avoid the effect of the accumulative salts stemming from the earlier saturation, the measurements were performed from the lowest to the highest salinity. Water was injected into the sample until the electrical conductivity of the output water was stable and in equilibrium with that of the input. For clay-bearing mixtures having clay content from 15% to 35%, water injection within the column was impossible because of the low permeability of the sample. Therefore, we saturated the sample with the respective solutions before inserting them into the sample column.

In addition, the recorded electrical conductivity values were also corrected for temperature (Campbell et al., 1948; Hayasi et al., 2004; Hermans et al., 2014; Hermans et al., 2015; Colombano et al, 2019) to expected standard conditions (commonly 25^0C) due to the linear relationship between the conductivity and temperature as follows:

$$\sigma_{rec} = \sigma_{cor}\,[1 + a_{cor}\,(t_{rec} - t_{cor})] \qquad (1)$$

where σ_{rec} (in S.m^{-1}) is the electrical conductivity recorded in saturated conditions at the temperature t_{rec} (°C) and σ_{cor} (in S.m^{-1}) is the corrected electrical conductivity at t_{cor} (°C), a_{cor} represents the slope in the variability of electrical conductivity per degree Celsius, and varies in a thermal range from 0.018 to 0.023 (^{0}C^{-1}). We corrected all measurements to 25°C using a_{cor}= 0.02 ^{0}C^{-1}.

The complex conductivity and phase shift are investigated at an input voltage of 5 V and the frequency in an interval range from 1 Hz to 45000 Hz. However, during processing, we prioritize the low-frequency range under 1000 Hz, particularly at 1 Hz due to their stability and sensitivity to salinity. For all salinities, three replicates were investigated. We also measured both reciprocal and normal measurements to estimate the error. The reciprocal measurements were performed prior to normal measurements. A reciprocal measurement is a procedure where current and potential electrodes are switched. The voltage difference applied during the reciprocal measurement was of lower intensity to stay close enough to the current-free electrode impedance. It was usually ±0.1 V instead of ±5 V (Huisman et al., 2016).

An essential point in the evaluation of the complex electrical conductivity is the assessment of the geometrical factor of the sample holder (Revil et al., 2017; Revil at al., 2021). To translate a measured complex impedance to a complex electrical conductivity, this factor depends on the position of electrodes which affects the current distribution between the current electrodes and the geometry of the sample holder. We determined the geometric factor by filling the column with the saline solutions of known conductivity only (no solid matrix) and measuring the impedance with the mentioned-above SIP configuration. The geometrical factor of our sample holder is 0.01357 m.

3.1.2. Sample preparation

Particle size distribution analysis (PSD) (Wentworth, 1922) using both wet and dry standard sieving techniques as stipulated in the American Society for Testing and Materials (ASTM D422-63) was first applied to sort unconsolidated sediments. Fifty-five disturbed samples collected from ten drilled boreholes coinciding with the geophysical measurements (Fig. 1) were classified into four groups: three clay-free categories composed of clean sand (fine-, medium-, and coarse-grained sand) and a clay-bearing mixture category. In addition, the finer suspended particles of the 2 µm fraction were analyzed through X-ray diffraction revealing the mineralogical content of the clay fraction mainly contains an aggregate of kaolinite, illite, chlorite, and a smaller quantity of goethite (Table 1).

Table 1: Summary of the results of X-ray diffractograms

Order. No	**Sample. No**	**Mass (gram)**	**Components and content (%)**						
			Illite	***Kaolinite***	***Chlorite***	***Quartz***	***Potassium Feldspar***	***Goethite***	***Others***
1.	LK07-BT (0-13m)	58.31	18-20	7-9	1-3	51-53	9-11	4-6	-
2.	LK07-BT (13-15m)	58.46	15-17	12-14	3-5	48-50	8-10	3-5	Amphibole, Lepidolite, Calcite

3.1.3. Complex conductivity (σ)

The complex conductivity (σ) can be expressed as :

$$\sigma(\omega) = \sigma'(\omega) + i\sigma''(\omega) = |\sigma|e^{i\varphi} \quad (2)$$

with $|\sigma| = \sqrt{\sigma'^2 + \sigma''^2}$ the amplitude, $\varphi = atan\frac{\sigma''}{\sigma'}$ the phase shift, σ' the real or in-phase component related to the ohmic conduction properties and σ'' the imaginary or out-of-phase component linked with the capacitive and inductive properties. For small phase shifts as the ones observed for consolidated and porous sediments (<100 mrad), phase shifts can be estimated as the ratios:

$$\varphi_r(\omega) \approx \left(\frac{\sigma''(\omega)}{\sigma'(\omega)}\right) \quad (3)$$

This approximation is fairly valid for metal-free soils and rocks (Kemna, 2000; Schön, 2011; Heenan et al., 2013; Saneiyan et al., 2018).

At low frequencies comparable to field surveys of time-domain IP (<10 Hz), we may neglect the effect of the complex permittivity ε^* so that the effective in-phase conductivity and the effective quadrature conductivity corresponds to σ' and σ'' (Kremer et al., 2016). For higher frequencies, the displacement current has to be taken into account through the dielectric permittivity.

When electronic semi-conduction or metallic conduction can be neglected, i.e. in the absence of metal-bearing grains, the conductivity may be described in terms of the electrolytic conduction σ_{el}, which may be regarded as affecting only the real part of conductivity in parallel with interfacial or surface conduction (σ_{int}), which affect both the real and the imaginary parts of conductivity (Kemna, 2000).

$$\sigma = \sigma_{el} + \sigma_{int} \qquad (4)$$

The conductivity of the material σ_{el} (at full saturation) is commonly expressed for saturated media as (Archie, 1942; Winsauer et al., 1952; Schön, 2011):

$$\sigma_{el} = \frac{\sigma_f}{F} = \frac{\Phi^m}{a}\sigma_f \qquad (5)$$

where the formation factor ($F = \frac{a}{\Phi^m}$) is inversely proportional to pore textural properties, namely the cementation exponent (m) and porosity (Φ) (Schön, 2011), while a is an empirical factor that should be equal to one, and σ_f refers the pore fluid conductivity.

3.1.4. Correlation between time-domain chargeability and complex electrical quantities

It is standard to fit a Cole-Cole model to relate the induced polarization effects in the time domain with the observations in the frequency domain (Everett, 1997). Indeed, the Cole-Cole model is an accepted complex conductivity/resistivity model expressed by the normalized chargeability (M_n), the frequency dependence (f or ω), and the time constant (τ) (Cole and Cole, 1941; Kemna, 2000) as follows:

$$\sigma_c = \sigma_\infty - \frac{M_n}{1 + (i\omega\tau_0)^c}$$

$$M_n = \sigma_\infty - \sigma_0 \geq 0 \tag{6}$$

Herein, M_n is the normalized chargeability, defined as the geometric mean frequency derived from the disparity in electrical conductivity at low frequency (σ_0) and high frequency (σ_∞), and c denotes the frequency exponent within the range $0 \leq c \leq 1$. Additionally, τ_0 represents the relaxation time (or time constant) measured in seconds. As described by Revil et al. (2017), the normalized chargeability is intricately associated with the quadrature conductivity, specifically measured at or close to the relaxation peak (Revil et al., 2017; Vinegar and Waxman, 1984). Revil et al. (2017) found the normalized chargeability to be linked to the quadrature conductivity by:

$$M_n \approx -(\frac{2}{\pi} lnD)\sigma'' \tag{7}$$

where $logD$ denotes the number of decades between low and high frequencies. M_n is therefore proportional to σ''(Revil et al, 2015). The slope of this linear relationship is related to the frequency interval.

$$\sigma'' \approx -\frac{M_n}{\alpha} \tag{8}$$

$$\alpha \approx \frac{2}{\pi} lnD \tag{9}$$

In this paper, assuming that the investigated range from low to high frequency corresponds to four decades ($D=10^4$), the frequency constant of 5.87 is chosen to assess a threshold value on the normalized chargeability for the detection of clay.

3.2. Field measurement

3.2.1. ERT and TDIP measurements

ERT and TDIP imaging were performed on 7 profiles collected in both upstream and downstream parts along the Luy River. All mid-points of profiles coincide with the boreholes where the samples for laboratory analysis were collected (Fig. 1).

With the goal of validating the petrophysical relationship accounting for clay and obtaining a good signal-to-noise ratio, the ABEM Terrameter LS1 equipment using dipole-dipole configuration including 64 electrodes was used in each profile with 2.5 m and 4 m separation between electrodes depending on the depth of the drilled boreholes. The minimum and maximum currents were 10 mA and 500 mA respectively. The acquisition delay time was set up at 0.8 seconds and the acquisition time to 1.2 seconds resulting in a total injection of 2 seconds. The TDIP signal was recorded using 20 time windows using increasing time intervals for a total recording time of 4.0 seconds. To reduce the contact resistance and maintain a reliable signal-to-noise ratio throughout the investigation sequences, saltwater was poured at the locations of the electrodes buried under dry sand conditions. The acquisition protocol was sorted to avoid the electrode polarization effect (Dahlin et al., 2002).

Prior to inversion, the negative resistance values and chargeability exceeding 1000 mV/V, that are considered physically impossible (Loke, 2011) were removed, and noisy decay curves were removed manually (Evrard et al., 2018). Relying on the methodology proposed by Slater et al. (2000), data quality was also assessed for 6 profiles based on reciprocal measurements. A threshold of 1% was selected to filter the data sets for all profiles, except for the reciprocal error in profile LK19-BT, for which 5% was selected. The dataset is inverted in RES2DINV (Loke and Baker, 1996). The L1-norm was used for both the model constraint to promote sharper resistivity contrasts (Cong-Thi et al., 2021a) and the data constraint to limit the impact of possibly remaining outliers.

3.2.2. Electromagnetic logs

Electromagnetic induction (EM-log) was used to collect vertically detailed logs of the electrical conductivity in 9 drilled boreholes equipped with non-conductive PVC casing

(Vandenbohede et al., 2008). The EM39 probe (from Geonics ©.) that operates at a frequency of 39.2 kHz with a coil spacing of 0.5 m was used (Mc Neill, 1990).

Before each logging, the calibration procedures were applied to verify that the probe was solely measuring zero conductivity. Data were collected in the vertical direction using a distance interval of 0.2 m. The collected data were validated in both up and down directions. The inner diameter of the boreholes is 60 mm, which should minimize the influence of the borehole fluid and casing, as the probe's sensitivity is maximum at a radial distance of 30 cm from the probe center (McNeil et al., 1990).

4. Results

4.1. Laboratory results

4.1.1. SIP

Figures 2a and b show a significant influence of the NaCl concentration on the spectra of both real (σ') and imaginary (σ'') conductivity. The dependence of the out-of-phase component is observed at frequencies higher than 1000 Hz (Fig. 2b). As expected, higher saline concentration corresponds to higher magnitudes of complex conductivity (Fig. 2a), whereas the opposite trend is observed for the phase (Appendix B). In addition, no peak is observed in the complex conductivity spectra. This might be explained by the non-uniform grain size of the sandy materials. Figure 2c and d illustrate the influence of the presence of clay minerals, increasing both the real and imaginary conductivity components, particularly for low salinity. This increase is dependent on the clay content of the samples.

The sample containing 35% has a lower conductivity than expected, this could be caused by an increase in the cementation exponent. Natural clay in sediments can play a considerable role as cement in the pore space of sandy sediments, resulting in reducing the porosity and pore-connectivity, particularly surface ionic mobility. Furthermore, the surface conductivity caused by charged ion mobility in the EDL dominates the complex conductivity. This phenomenon also affects the quadrature conductivity component. In other words, the mixture containing a large proportion of clay minerals seems to be more compacted, reducing the cation exchange capacity (CEC) of clay. This effect might have been induced by the sample preparation.

The Cole-Cole model approach was used to fit the measured SIP curves of all clay-free and clay-bearing categories using PyGIMLi (Rücker et al., 2017). Figures 2e and 2f show the IP spectra of the representative samples for fine sand and clayey sand (25% clay), with the c exponent equal to 0.5. The decomposition fits the curve of fine sand more accurately than that of the clay-bearing sample. For the imaginary component, except for the well-fitted spectra of the quadrature component under 1000 Hz, a partition of the spectra is not well-fitted by the Cole-Cole model at frequencies above 1000 Hz. The reason could be the potential effect of the roughness of the grains in polarization conditions of the grain-pore water interface and the dielectric effect (Leroy et al., 2008; Revil et al, 2014).

Figures 2g and 2h illustrate the two-phase component spectra of real and quadrature conductivity on time scales. A peak is observed in the spectrum of the fine sand sample in a time interval of 1-2 ms, which is the relaxation time τ_{50} at which 50 percent of the total chargeability is reached (Weigand and Kemna, 2016). Inversely, no clear dominant relaxation time is observed for the broad grain-sized clay-bearing sample. As mentioned earlier, this might be associated with the surface roughness effects and the superposition of particles, widening the relaxation time (Sara Johansson, 2020).

The normalized chargeability is also plotted against time as a cumulative curve and the quadrature conductivity (Eq. 9, Fig. 2i and j). In the investigated frequency of four decades, the general tendency between the normalized chargeability and quadrature conductivity is a linear relationship with a slope of 5.98. The normalized chargeability varies proportionally with the increased clay content. For the low-frequency range, a threshold value for the normalized chargeability around 1 mS.m^{-1} can be deduced to validate the presence of clay.

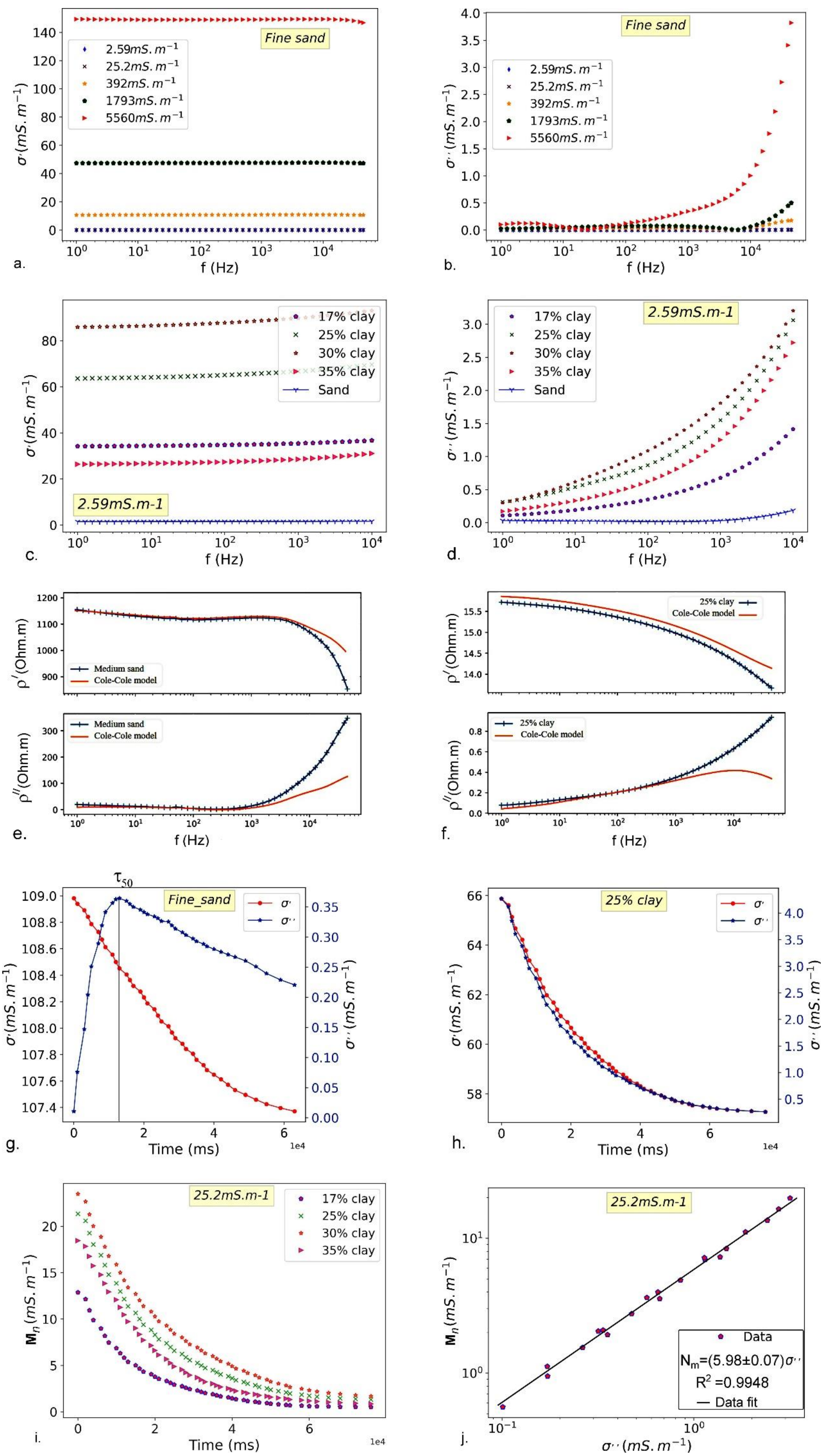

a.
Fine sand
2.59mS.m-1
25.2mS.m-1
392mS.m-1
1793mS.m-1
5560mS.m-1
σ'(mS.m-1)
f (Hz)
b.
Fine sand
σ''(mS.m-1)
f (Hz)
c.
17% clay
25% clay
30% clay
35% clay
Sand
2.59mS.m-1
σ'(mS.m-1)
f (Hz)
d.
2.59mS.m-1
σ''(mS.m-1)
f (Hz)
e.
Medium sand
Cole-Cole model
ρ'(Ohm.m)
ρ''(Ohm.m)
f (Hz)
f.
25% clay
Cole-Cole model
ρ'(Ohm.m)
ρ''(Ohm.m)
f (Hz)
g.
τ50
Fine_sand
σ'
σ''
σ'(mS.m-1)
σ''(mS.m-1)
Time (ms)
1e4
h.
25% clay
σ'(mS.m-1)
σ''(mS.m-1)
Time (ms)
1e4
i.
25.2mS.m-1
17% clay
25% clay
30% clay
35% clay
Mn(mS.m-1)
Time (ms)
1e4
j.
25.2mS.m-1
Data
Nm=(5.98±0.07)σ''
R2 =0.9948
Data fit
Mn(mS.m-1)
σ''(mS.m-1)

Figure 2. a. The in-phase (σ') and b. out-of-phase (σ'') conductivity components of the representative clean sand category for different salinities. Effects of clay content with respect to the surface conductivity at the lowest salinity, corresponding to deionized water on the amplitude of the in-phase (c) and out-of-phase components (d). Fitting with the Cole-Cole model for fine sand (e) for 25% clay-bearing sand (f). The peak of the synthetic SIP data in terms of real and quadrature conductivity, for fine sand (g) and clay-bearing sand (h). Normalized chargeability against time (i) and quadrature conductivity (j) in log values, with frequency constant α = 5.87, the best fit data (5.98±0.07).

4.1.2. Petrophysical relationship

To estimate the relation between the real conductivity, the pore fluid conductivity, and the interfacial conductivity, we rely on equations 4 and 5. Figure 3a shows two different trends for clay-bearing and clay-free samples. For the clean sand category, a nearly linear dependence of the in-phase conductivity on the pore water conductivity is observed. Inversely, a non-linear relationship is clearly observed in the clay-bearing mixtures, particularly for low salinities where surface conductivity even dominates due to mobile ions in the EDL. The general tendency of the relationship observed is a linear portion at high salinity with a non-linear transition at lower salinities where the curve approximately approaches a constant, which represents the surface conductivity at low salinity.

The increased clay content in the range 17%-30% yields a growing influence of the surface conductive values on the amplitude of the intercept as observed in Fig. 3b. The sample with 35% clay does not follow this trend as explained above.

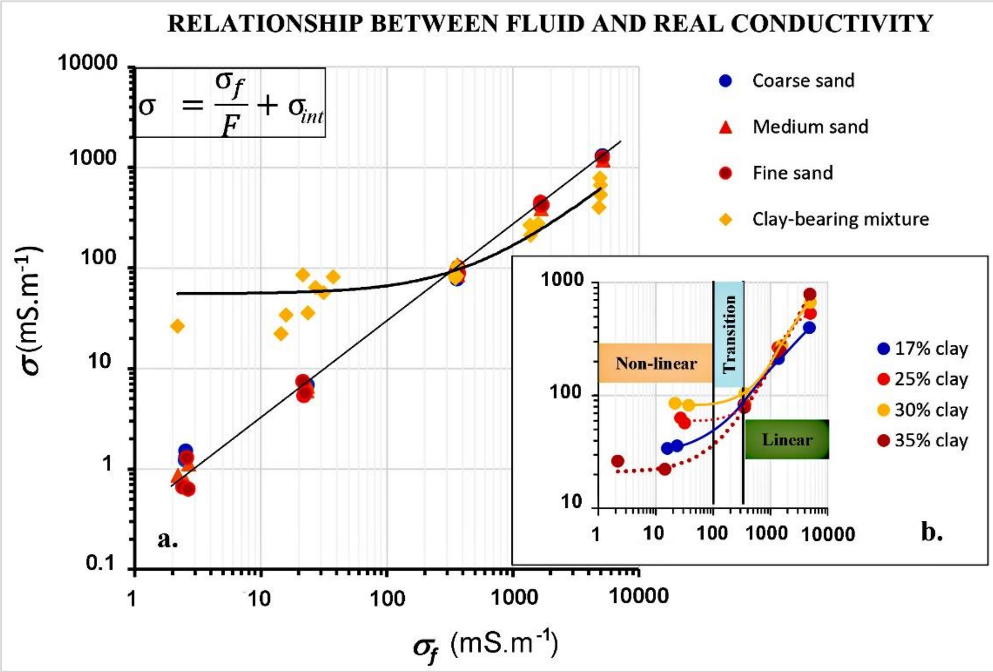

Figure 3. Log-log plot of the pore fluid conductivity versus the real conductivity. (a). A straight line represents the clean sand category (including coarse-, medium- and fine particles) and a curve refers to the clay-bearing mixture. (b). The generally detailed trends between σ and σ_f of four clay-bearing samples indicate linear relationships at higher salinity and non-linear relationships at lower salinity.

The formation factor F is the reciprocal of the slope in the linear portion, and the surface conductivity σ_{int} is the intercept part. (Table 2). The surface conductivity of clay-bearing sand is up to 40 times larger than that of clay-free sediments.

Table 2. Formation factor and surface conductivity of four sedimentary groups in the Luy River

Category		**F**	**σ_{int} (mS.m^{-1})**
Clay-free sediments	Coarse sand	4	2
	Medium sand	4.4	6
	Fine sand	4.1	5
Clay-bearing sediments	17% clay	13.4	55
	25% clay	10.3	71
	30% clay	8.3	76
	35% clay	6.4	21

	Mean	8.9	55

Based on the petrophysical relationship, it is possible to define resistivity threshold values corresponding to freshwater and saline water transitions (based on 1000 and 3000 mg/L TDS limits, Cong-Thi et al., 2021a) for the four porous sediment groups calculated using equations 4 and 5 and the fitted parameters. Water electrical conductivity is converted into TDS values using a linear relationship (Keller et al., 1966; Cong-Thi et al., 2021a). Due to the uncertainty in the formation factor resulting from the different samples, we use conservative rounded threshold values (Table 3). For the sand categories, resistivity under 9 Ohm.m corresponds to saline conditions (> 3000 mg/L), and resistivity above 25 Ohm.m indicates freshwater (< 1000 mg/L). The intermediate interval corresponds to brackish water. Analogously, the threshold values for the clay-bearing mixture are 9 Ohm.m and 14 Ohm.m for saline and freshwater conditions respectively. Remarkably, these values are in agreement with the estimation of Cong-Thi et al,. (2021a) made in the absence of co-located data. The threshold to be used for freshwater depends on the normalized chargeability (14 Ohm.m if M_n>1 mS.m^{-1}, 25 Ohm.m otherwise).

Table 3. Resistive threshold values for the Luy River sediments in different salinity conditions

Category	**Resistivity threshold (Ohm.m)**	**Condition**
Clay-free sediments	>25	Fresh
	9-25	Brackish
	<9	Saline
Clay-bearing sediments	>14	Fresh
	9-14	Brackish
	<9	Saline

4.2. Field results

4.2.1. Resistivity and TDIP

Assuming that laboratory samples are representative for field conditions, the threshold values computed at the laboratory scale can be used for the field scale interpretation, and combined with borehole logs to characterize the complex distribution of heterogeneous sediment sequences. Examples are given in Fig. 4 and 5 for two selected profiles (IP07 and IP03). Near the surface, since unsaturated and freshwater conditions dominate, the observed resistivity varies laterally from 5 Ohm.m to 45 Ohm.m in both profiles, indicating clay-dominated lithology as confirmed by the respective lithologs (LK07-BT and LK03-BT). Deeper, in IP07 lower resistivity values varying from 1.5 Ohm.m to 3 Ohm.m are visible at depths from 5 m to 14 m. The lithology is relatively homogeneous, corresponding to sandy clay under saline conditions. The high values of the normalized chargeability observed at the bottom of the borehole in IP07 might be related to the high clay content along the whole litholog although the presence of artefacts of inversion is possible given the amplitude of the anomaly. Nevertheless, normalized chargeability higher than 1.5 mS.m are consistently observed along the first half of the profile.

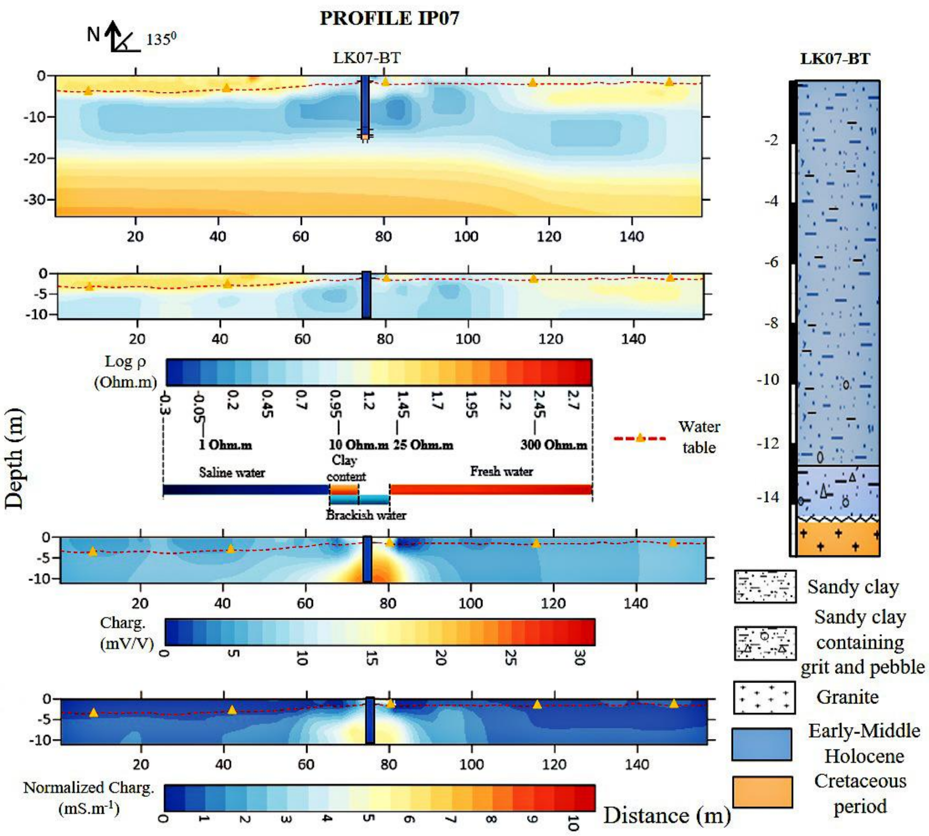

Figure 4: Inverted resistivity, chargeability and normalized chargeability of IP07 in correlation with lithostratigraphical logs in boreholes LK07-BT. Lower is the mapping of chargeability/ normalized chargeability. The broad variation of chargeability in profiles shows the more complicated distribution of clay content in the inhomogeneous context of lithology. Root-mean-squared (RMS) errors of IP07 chosen at 5 consecutive iterations are 1.28% and 0.96% in resistivity inversion and in chargeability map, respectively.

In IP03, a decrease of resistivity values at depths between 3 m and 15 m from 16 Ohm.m to 4 Ohm.m from the right part to the left part of the figure 5 seems inversely proportional to the higher clay content, as corroborated by the higher normalized chargeability from 3 $mS.m^{-1}$ to approximately 4.5 $mS.m^{-1}$. This reveals that surface conduction mechanisms of disseminated clay particles play a significant role in low resistivity.

The transition between the unconsolidated sediment layers and unaltered bedrock is characterized by the rapid increase of the resistivity responses from 50 Ohm.m to 150 Ohm.m (Fig. 4 and 5). These values are extremely low for what is expected to be unaltered granite (> 1000 Ohm.m) (Lowrie, 2007). The main contributor to this lower signal is the presence of fracture-filled salty groundwater. The clay content also increases at the transition between unconsolidated sediments and the lower-lying bedrock, which is composed of an upper altered granite zone. Typically, the unaltered bedrock is identified by an increase in resistivity and low normalized chargeability, while it is currently shown by the normalized chargeability varying from 1.5 $mS.m^{-1}$ to 3 $mS.m^{-1}$ and relatively low resistivity. Particularly in the complexity of predominantly saline conditions, other contributors decreasing the conductivity could be overshadowed. Herein, saltwater is the main contributor while clay presence is a co-contributor.

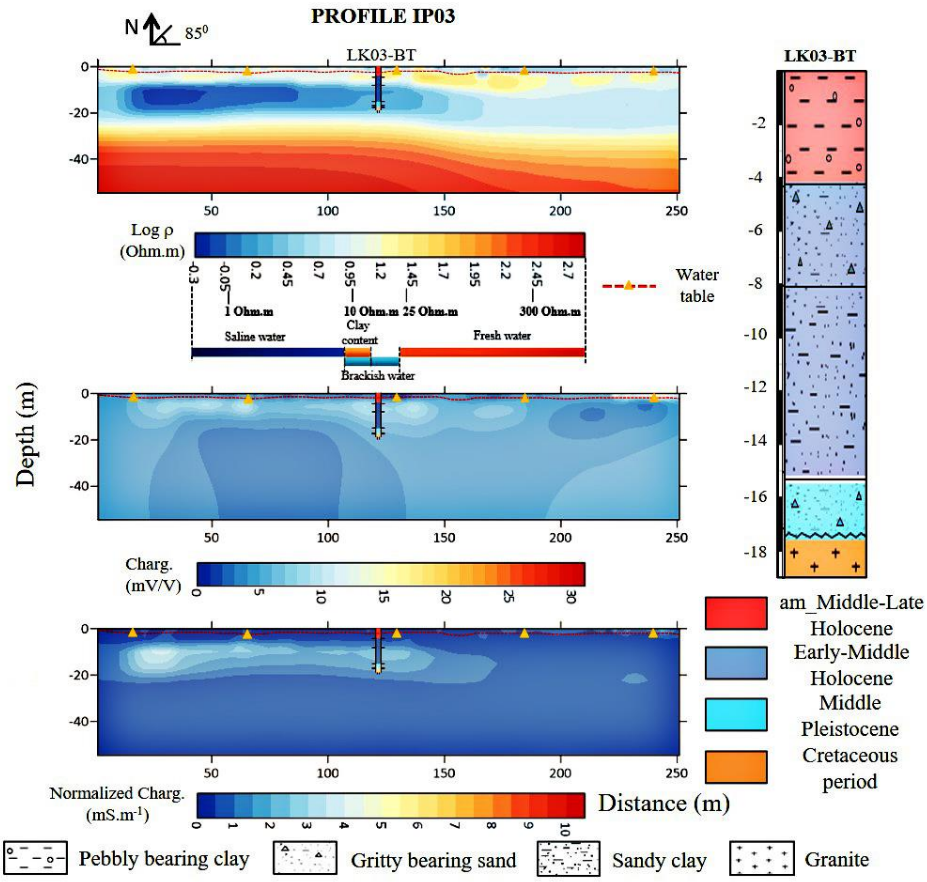

Figure 5: Similar to IP07, the inverted resistivity, chargeability and normalized chargeability of IP03 in correlation with lithostratigraphical logs in boreholes LK03-BT. Lower is the mapping of chargeability/ normalized chargeability. Higher normalized chargeability indicates the presence of clay content. Root-mean-squared (RMS) errors of IP03 chosen at 5 consecutive iterations is 0.97% and 0.44% in resistivity inversion and in chargeability maps, respectively.

4.2.2. Correlation between EM-logs and ERT data

To validate the variations of the resistivity in the heterogeneous sediment layers, we provide a comparison of the inverse solutions with co-located data by computing the average recorded value in EM-logs within the corresponding ERT grid cells. Averaging within a grid cell allows to partly account for the different investigated volumes (Benoit et al., 2019).

Overall, ERT can reproduce relatively well the conductivity trend measured in logs (Fig. 6 and 7). Better matching between both measuring techniques is visible at low conductivity intervals from 0 to 250 $mS.m^{-1}$ (Fig. 6a), corresponding to fresh-brackish water conditions (TDS < 1500 mg/L, Appendix C). Most ERT-inverted conductivity values (approximately 70%) have a deviation smaller than 30 mS.m^{-1} from what is measured at a higher resolution with EM-log (Fig. 6a). This good correspondence is for example observed in LK07-BT and the shallower location (< 20 m) in LK01-BT. The ERT values correctly image the gradual increase in conductivity from 150 mS.m^{-1} in LK07-BT and 80 mS.m^{-1} in LK01-BT at the depth of 8 m to higher conductivity at larger depths (Fig. 7a and b), corresponding with what is expected in theory for clay-dominated sediments. This reveals the conductive response being governed by lithology.

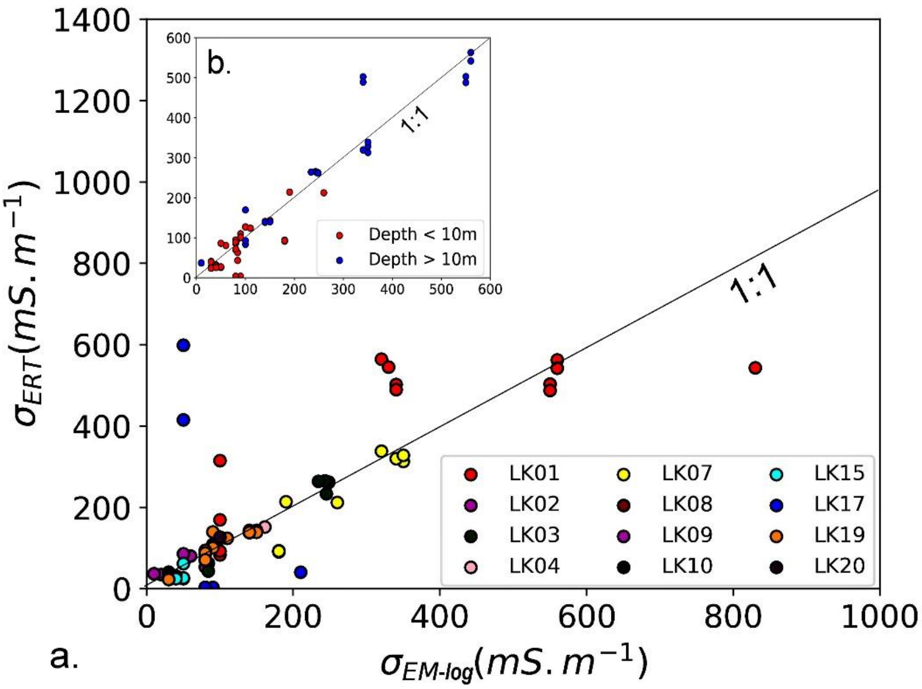

Figure 6. a. Relationship between EM-logs and ERT dataset. The 1:1 lines represent perfect correlations. b. Correlation between EM-log and ERT with depth. The depth division is chosen as 10m based on the averaged mid-depth point of each profile.

Nearly 20% of the total investigated points have a difference of 30 - 100 mS.m^{-1}. Such difference is for example observed between 4 m and 6 m deep in LK03-BT (Fig.7b), where a decrease in conductivity is shown from 85 mS.m^{-1} to 40 mS.m^{-1}, relatively consistent with the transition to a coarser category containing a majority of sands and a minority of clay and grit (< 15%) in the lithologs. In contrast to EM-logs at this deep interval, the observed ERT values are only varying in a limited range from 45 mS.m^{-1} to 65 mS.m^{-1}. This discrepancy could be related to the limited resolution of the inversions.

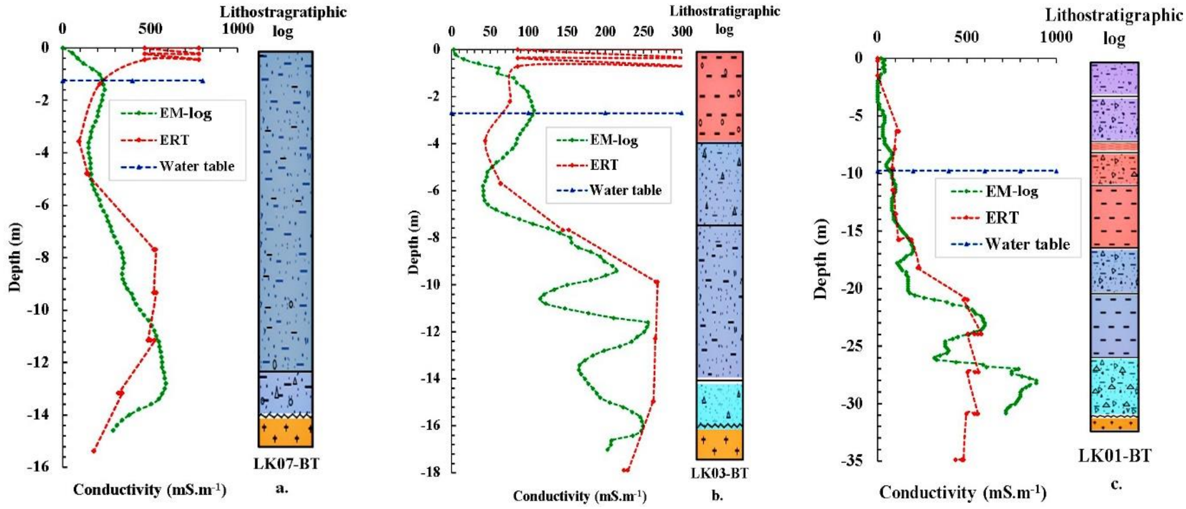

Figure 7. Conductive relationship between EM-logs and ERT dataset.

The tendency of increase in conductivity downward to the bedrock, due to increased salinity in groundwater (Fig. 7), is observed in most EM-logs. However, this trend is not always consistent in inverted models, leading to high differences exceeding 100 mS.m^{-1}. A typical example is for the unconsolidated layers lying on granite bedrock, in LK01-BT (Fig. 7c), the increase in conductivity of EM-log reaches 900 mS.m^{-1} in the gravel layer while that of ERT is much lower (around 500 mS.m^{-1}) and varies insignificantly below the depth of 20 m. The high deviations for these data are caused by the regularization term and loss of the resolution with depth (Day-Lewis et al., 2005; Hermans and Irving, 2017), and sometimes to compensation artefacts (higher resistivity spike causing lower resistivity values below, see for example the obvious outlier in LK07-BT). These effects prevent ERT to provide an as detailed description as combined EM/lithologic logs. However, there is no clear indication that the depth can explain strongly deviating points (Fig. 6b). This implies that a diminishing depth resolution is not the only cause for deviations, but other causing factors such as the presence of inversion artefacts caused by anthropic structures at the surface, the averaging calculation methodology, and the measuring scale play a role. High deviations are also observed near the surface, at depths shallower than 1 m, conductive features in the ERT data fluctuate repeatedly from 80 mS.m^{-1} to 300 mS.m^{-1} in LK03-PT and from 450 mS.m^{-1} to 800 mS.m^{-1} in LK07-BT while EM-logs in both boreholes varies slightly under 150 mS.m^{-1}. This could be related to global smoothing regularization and the above-mentioned artefacts of inversion linked to anthropic structures in the vicinity of the wells (Hermans and Irving, 2017; von Bülow et al., 2021).

Generally, the ERT and EM-log features show relatively identical trends but ERT data is recorded through a larger scale and with a lowering resolution with depth, causing deviations from EM-log data. For conductivity values under 250 $mS.m^{-1}$ corresponding to fresher conditions, the ERT inverted models reveal a more accurate quantitative estimation of the bulk electrical conductivity. For higher conductivity values, the ERT inversion models are qualitatively correct and generally sufficient to conclude the resistivity threshold for saline water that has been reached.

4.2.3. Correlation between salinity and ERT data

Figure 8 shows two scatterplots comparing salinity translated into fluid conductivity and bulk conductivity for clay-free and clay-bearing layers. We extracted ERT conductivity values in boreholes where the water conductivity was measured on groundwater samples. The bulk inverted resistivity at the depth of the screen interval was averaged within a 5 m radius cylinder around the borehole location.

Figure 8a represents the sandy sediment. Most points have a water conductivity lower than 250 $mS.m^{-1}$, related to their position in relatively fresh part of the aquifer, which makes it difficult to derive a strong trend for a broad range of salinities. Most points show a spread around the linear trend line at low conductivity values. Analogously to the lab methodology, from equation 4, the formation factor and surface conduction can be derived and are 3.8 and 40.201 $mS.m^{-1}$, respectively. The surface conductivity value is larger than in the lab and likely accommodates the averaging nature of resistivity at this scale.

Figure 8b corresponds to clay-dominated samples. Here, data points are scattered over a wide range of bulk electrical conductivity for a given water conductivity. This scattering is likely an effect of the variability in the clay content of the various samples, in accordance with what was observed for the surface conduction of laboratory samples, combined with the averaging effect of

ERT. Although deriving a trend is only indicative given the weak tendency, a formation factor of 8.1 and surface conductivity of 105.24 $mS.m^{-1}$ are derived.

Remarkably, the spread in bulk conductivity observed at the low value of water conductivity is consistent with the expected range observed at the laboratory scale (Fig.3, Table 2), spanning almost one order of magnitudes. Similarly, the formation factor values are acceptable for the described lithology and in agreement with lab processing data. However, the field-scale surface conductivity is higher than the lab-scale one. This is likely related to the heterogeneous nature of the sediment sequences in the study area (Fig. 4, 5 and 7). Indeed, the broad grain-sized variation, fraction and dispersion of clay are responsible for deviations from the lab petrophysical relationship.

The good agreement of ERT with EM-logs at low salinity combined to the large spread observed in the field petrophysical relationship suggests that the clay content has an important impact on the field resistivities. ERT results can therefore be used for qualitative saltwater delineation (high salinity threshold), but should be thoughtfully handled to derive quantitative estimates of the salinity, especially at low salinities, where the clay content dominates the response.

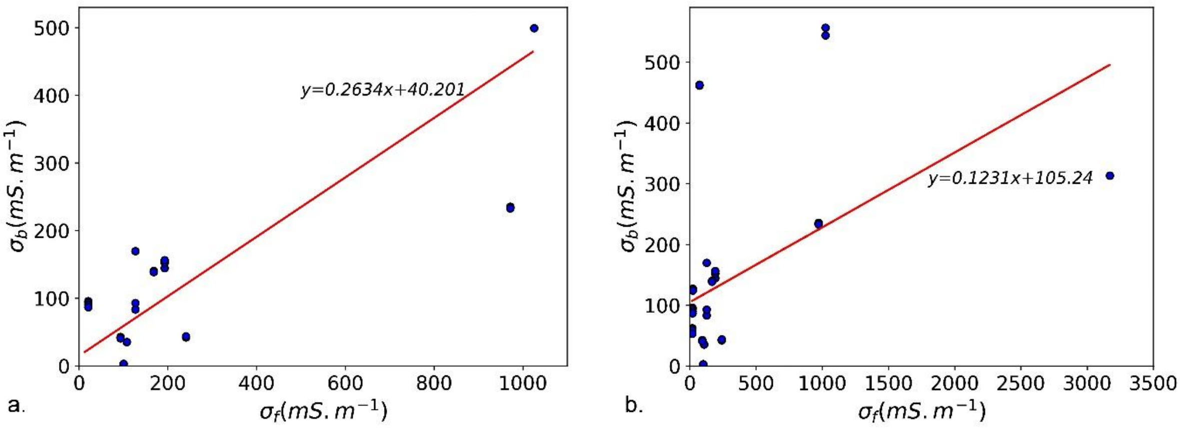

Figure 8. Plotting fluid conductivity against bulk conductivity. a. For the clay-free category. b. For the clay-bearing mixture.

5. Discussion

The combination of ERT/TDIP and EM-logs at the field scale with SIP investigations and lithological description at the laboratory scale has allowed us to derive clear threshold values for the interpretation of electrical properties in terms of salinity and heterogeneity.

At the small scale, our laboratory data shows that the normalized chargeability is proportional to the electrical surface conductivity of samples and increases with the clay content (Fig. 2c, 9a and b), which is known to be correlated with the cation exchange capacity used in complex conductivity models (Revil et al, 2017). A threshold of the normalized chargeability value of 1 $mS.m^{-1}$ appears to be a suitable criterion for discerning the substantial presence of clay minerals. At the field scale, we have observed relatively low values of normalized chargeability, ranging from approximately 0.7 $mS.m^{-1}$ to 1.3 $mS.m^{-1}$, in areas where lithological analysis indicates a low clay content (<15% clay), while values ranging from 3 to 10 $mS.m^{-1}$ are characteristics of clay layer and lenses (see Fig. 4, 5, and 9c, d). These observations align with the normalized chargeability and percentage of clay minerals obtained through the SIP investigations and comprehensive lithological descriptions, respectively. The analysis of normalized chargeability, when compared with the X-ray diffractograms and EM-logs, has revealed an intricate distribution pattern of clay minerals predominantly composed of kaolinite and illite. These minerals exist in various formations within the subsurface as discontinuous small lenses, occasionally with brackish or saline porewater, or as more continuous layers with thicknesses ranging from 0.5 m to 5.5 m, acting as regional aquitards (see Fig. 5). Furthermore, clay minerals are frequently dispersed within the sand layers, as illustrated in Figures 4, 5, and 7.

Consequently, the use of normalized chargeability assists in distinguishing between clay content and salinity within the resistivity response. Figure 9 shows an example of how laboratory results can be used to extract both clay content and salinity out of the ERT-TDIP measurements at the field scale. Laboratory measurements are identifying a linear relationship between normalized chargeability, clay content, and surface conductivity (Fig. 9a). This allows translating the TDIP inversion into a clay content map (Fig. 9c), validated with co-located measurements (Fig. 9b). The

TDIP inversion also allows to estimate a spatially distributed surface conductivity, that is then used to locally estimate the salinity (Fig. 9d) based on the petrophysical model (Equation 4, Fig. 3). Figure 9 illustrates that high clay content areas tend to retain saltwater leading to globally higher salinity in clay-rich zone. This is in agreement with the conceptual model for saltwater intrusion in the study area based on hydrochemical analysis (Dieu et al., 2022). The lack of sufficient co-located samples has impeded the validation of a definitive relationship between normalized chargeability and clay content at the field scale due to insufficient stacking or low SNR that have required to re-assess the field acquisition parameters. This can be avoided by ensuring a proper SNR although this is more challenging in high salinity conditions.

The laboratory samples allowed for deriving clear petrophysical relationships for sandy and clay-bearing sediments with consistent formation factors. The surface conductivity is one order of magnitude larger for the latter, as expected. This approach allowed us to derive threshold values for saline and fresh water for both sediment types (Table 2). The latter appeared to be successful in delineating saline zones on the field and were also consistent with previous studies (Cong-Thi et al., 2021a).

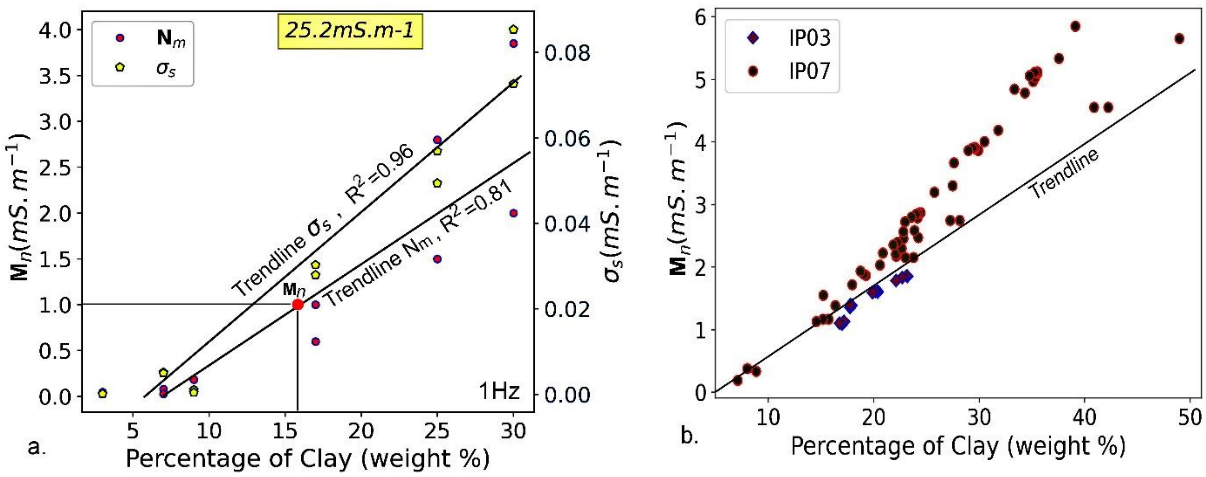

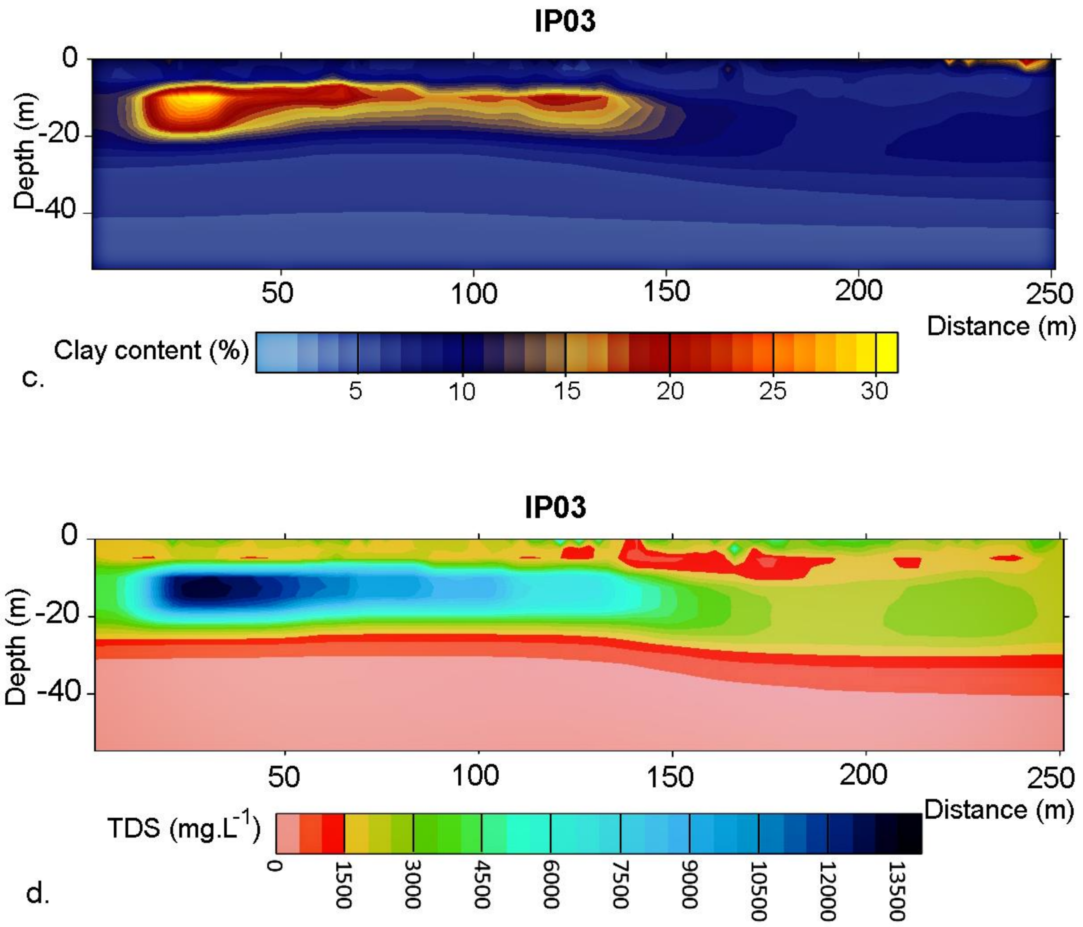

Figure 9. The relationship between the normalized chargeability and clay content which is shown as the weight fraction of finer particles of 2mm indicates linear dependence, a red point on the trendline of Mn is a threshold of 1 mS.m^{-1} (a). Note that the electrical polarization responses were conducted at the frequency of 1 Hz and in freshwater conditions. Plotting normalized chargeability versus clay content extracted from inversions IP03 and IP07 (b). Mapping for distributions of clay minerals percentage (c) and salinity (d).

The comparison with lithological logs, EM-logs and TDS measurements, at the field scale validated the formation factor obtained from the SIP investigation, while the field-scale surface conductivity values appeared higher than the lab-scale ones. The discrepancy could be related to the heterogeneous distribution of sedimentary layers, the coarser-sized aquifers that are alternating with argillaceous bands/lenses, and the existence of clay minerals dispersed within the pore space, causing an increase in surface conductivity magnitude. Besides, the local presence of ilmenite (Cong-Thi, 2021b), a conductive mineral, could affect the apparent increase in surface conductivity. Scale and inversion effects, leading to smoothing and averaging in the resistivity distribution, can also explain the presence of a significant surface conductivity for sand-dominated sediments. In addition, the absence of extremely saline samples at the field scale made the regression relatively sensitive to a few samples. The spread at low salinities is important, indicating the difficulty in deriving field-based petrophysical relationships in highly heterogeneous coastal aquifers. In the study area, in freshwater conditions (σ_f < 250 mS.m^{-1}, TDS < 1000 mg/L), bulk conductivity seems to be governed by the lithology, and the surface conduction mechanisms from clay particles dominate over ionic conduction.

EM-logs and ERT data generally display similar trends. However, ERT cannot detect thin clay sedimentary layers (less than 0.5 m in Fig.7c), due to the poorer vertical resolution. In this range of salinity, there is a very large spread in the field-based petrophysical relationship, corresponding to the large heterogeneity observed in the well logs, preventing ERT alone from making any quantitative interpretation because of the double effect of fluid salinity and clay content. In saltier conditions generally encountered at larger depths, ERT data still display the same trend as EM logs. However, ERT cannot systematically discriminate the transition between the complex sedimentary multi-layers (Fig. 7c) due to its volume-averaging nature of ERT and the loss of resolution with depth. Nevertheless, ERT seems to be consistent in predicting the salinity threshold of 9 Ohm.m for saline water (TDS > 3000 mg/L).

6. Conclusions

This paper investigated the electrical response of heterogeneous clay-bearing sediments subject to saltwater intrusion processes both in controlled laboratory settings and in-situ. Threshold values from SIP laboratory measurements for both the normalized chargeability and resistivity are combined at the field scale to identify clayey sediments from sandy sediments and within those two types of sediments, to apply the appropriate resistivity threshold to identify fresh from saline porewater. The results are validated with co-located logging data. The information obtained through SIP measurements therefore provides valuable insight into subsurface heterogeneity that may not be fully resolved through ERT and TDIP data only.

The findings from both the laboratory and field experiments exhibit a successful alignment with the established lithological structure as documented in borehole logs and also allow a more exhaustive interpretation of the lithostratigraphic correlation. As expected, the SIP data contribute significantly to the characterization of the surface conductivity of clay-containing sedimentary aggregates.

The outcomes of our investigation underscore the capability of SIP to discriminate lithological heterogeneities within unconsolidated sediments, particularly in the presence of clay minerals. The observed trends in surface conductivity values and formation factors, which increase from coarser sand to clay-bearing sand, closely adhere to theoretical expectations and closely resemble the results derived from field interpretations. Nevertheless, it is noteworthy that petrophysical relationships sourced from field observations exhibit considerable variability around the established trend, indicating that quantitative estimation is subject to large uncertainty. Linking petrophysical relationships at laboratory and field scales is typically considered to be well-established, particularly for characterizing formation factors in relatively homogeneous formations. Nevertheless, significant variations in surface conductivity are occasionally present in both clay-free and clay-bearing sand which can lead to large uncertainty when estimating the salinity. To maximize the correlation within the petrophysical relationship at both scales, it may be necessary to perform identical frequency measurements at both scales, accompanied by meticulous sample preparation in the laboratory and cautious data acquisition on the field.

The trends observed in EM-logs and electrical resistivity tomography (ERT) data within the field are reasonably consistent. Nevertheless, it is worth noting that the ERT data is recorded over a larger spatial scale with a lower vertical resolution, causing some deviations compared to EM-logs. These deviations can be caused by the regularization techniques employed during the inversion process and the loss of resolution with increasing depth. For sedimentary conditions characterized by low conductivity values, specifically for fresher conditions under 250 $mS.m^{-1}$, the ERT model provides a more precise quantitative estimation of the bulk electrical conductivity and can be used to detect the presence of clay constituents. However, quantitative interpretation remains challenging due to the combined effect of salinity and clay content. In such cases, the utilization of normalized chargeability proves beneficial in identifying the occurrence of clay lenses/ layers. For larger conductivity values, the ERT model is able to satisfactorily identify zones where the salinity exceeds the 3000 mg/L threshold. Nevertheless, it is imperative to emphasize that ERT should not be employed for deriving absolute salinity values in such scenarios.

The petrophysical analysis of the data acquired from SIP, ERT, and EM-logs investigations towards lithology and corresponding salinity pointed out the complexity linked to the very heterogeneous nature of the study area. Globally, the application of high-resolution ERT/IP inversions and EM logging has proven to be effective in discriminating the heterogeneity within clay-rich zones, even from saline-contaminated zones. Within clay-rich zones, the bulk electrical conductivity is amplified due to the concurrent presence of clay minerals and saline water, overshadowing the existence of clay-bearing strata, thereby sometimes mistaken for extreme salinity in the aquifers. Besides, ERT/TDIP data exhibits insensitivity to clay lenses or layers thinner than 0.5 meters, even at shallow depths. This insensitivity could potentially lead to misinterpretations, particularly in distinguishing between interbedded sand layers and saline or brackish conditions. In contrast, the ERT model provides a more accurate representation of the electrical response of the underlying bedrock.

Author Contributions: D.C.T conceptualized the survey plan, processed the ERT/ IP and SIP data and applied the methodology, and was responsible for writing the paper. L.P.D contributed to the fieldwork and data processing. D.C contributed to the methodology and SIP processing. X.D.P participated in the ERT/IP processing and EM-log comparison. H.D.T was responsible for sample preparation and do grain-sized analysis. H.H.H participated in the fieldwork and the conceptualization of the survey plan. N.F. and H.T conceptualized the survey plan and the methodology and supervised the study.

Funding: This research is funded by VLIR-UOS and the Belgian development cooperation through the grant VN2019TEA494A103, and theSpecial Research Fund (BOF), Ghent University through the Ph.D. scholarships of the first two authors.

Acknowledgments: We deeply thank the VIGMR staff for their support on the field and grain-sized classification. We would like to thank staff members in the laboratory of the Urban & Environmental Engineering, Liège University, who assisted us in the analysis of SIP measurements. We also thank André Revil and an anonymous reviewer for the pertinent remarks and suggestions leading to greatly improved manuscript. We would like to thank the Editor for supporting us in resubmission.

Conflicts of Interest: The authors declare no conflict of interest.

References

1. Alabi, A.A., Ogungbe, A.S., Adebo, B., Lamina, O., 2010. Induced polarization interpretation for subsurface characterization: A case study of obadore, lagos state. Archives Physics Research 1, pp. 34–43.
2. Archie, G.E., 1942. The electrical resistivity log as an aid in determining some reservoir characteristics. Trans AIME 146, pp. 54–62.
3. ASTM D422-63,. 2007. Standard Test Method for Particle-Size Analysis of Soils, ASTM International, West Conshohocken, PA.
4. Attwa, M., Günther, T., Grinat, M., Binot, F., 2011. Evaluation of DC, FDEM, and IP resistivity methods for imaging perched saltwater and a shallow channel within coastal tidal flat sediments. Journal of Applied Geophysics 75, pp. 656–670.

5. Baines, D., Smith, D.G., Froese, D.G., Bauman, P., Nimeck, G., 2022. Electrical resistivity ground imaging (ERGI): A new tool for mapping the lithology and geometry of channel-belts and valley-fills. Sedimentology 49, pp. 441–449.

6. Benoit, S., Ghysels, G., Gommers, K., Hermans, T., Nguyen, F., Huysmans, M., 2019. Characterization of spatially variable riverbed hydraulic conductivity using electrical resistivity tomography and induced polarization. Hydrogeology Journal 1, pp. 395–407. https://doi.org/10.1007/s10040-018-1862-7.

7. Börner, F.D., Schopper, J.R. and Weller, A,. 1996. Evaluation of transport and storage properties in the soil and groundwater zone from induced polarization measurements. Geophysical Prospecting 44(4), pp. 583–601.

8. Campbell, R., Bower, C., Richards, L., 1948. Change of electrical conductivity with temperature and the relation of osmotic pressure to electrical conductivity and ion concentration in soil extracts. Soil Sci. Soc. Am. J. 13, 66–69.

9. Changa, Yawen., X. Hua Bill., Xu, Zexuan., Lia, Xue., Tong, Juxiu., Chen, Lin., Zhang, Hanxiong., Miaoe, Jinjie., Liue, Hongwei., Mae, Zhen,. 2018. Numerical simulation of seawater intrusion to coastal aquifers and brine water/freshwater interaction in south coast of Laizhou Bay, China. Journal of Contaminant Hydrology, 215, pp: 1-10. https://doi.org/10.1016/j.jconhyd.2018.06.002.

10. Cole, K. S., and Cole, R. H., 1941. Dispersion and absorption in dielectrics. I. Alternating current characteristics, The Journal of Chemical Physics 9, pp. 341–351.

11. Cong-Thi, D., Dieu, L.P., Thibaut, R., Paepen, M., Huu, H.H., Nguyen, F., Hermans, T., 2021a. Imaging the structure and the saltwater intrusion extent of the Luy River coastal aquifer (Binh Thuan, Vietnam) using electrical resistivity tomography. Water 2021 13, 1743 pp. https://doi.org/10.3390/w13131743.

12. Cong-Thi, D., Pham Dieu, L., Huu Hieu, H., Nguyen, F., Hermans, T., 2021b. Granulometric and lithological composition of sediment in the boreholes along the Luy river in Bac Binh discs., Binh Thuan province: results and interpretation. Report. Ghent University, Belgium. Unpublished.

13. Dahlin, T., Leroux, V., & Nissen, J., 2002. Measuring techniques in induced polarisation imaging. Journal of Applied Geophysics 50, pp. 279–298.

14. Dahlin, T., and Leroux, V., 2012. Improvement in time-domain induced polarization data quality with multi-electrode systems by separating current and potential cables. Near Surface Geophysics 10, 1957 pp. https://doi.org/10.3997/1873-0604.2012028.

15. Day-Lewis, F.D., Singha, K., Binley, A., 2005. Applying petrophysical models to radar travel time and electrical resistivity tomograms: Resolution-dependent limitations. Journal of Geophysical Research 110, B08206. https://doi.org/10.1029/2004JB003569

16. Dieu, L.P., Cong-Thi, D., Segers, T., Huu, H.H., Nguyen, F., Hermans, T., 2022. Groundwater Salinization and Freshening Processes in the Luy River Coastal Aquifer, Vietnam. Water 14 (15), 2358 pp.

17. Dickinson, W.R and Suczek, C.A., 1979. Plate tectonics and sandstone compositions. American Association of Petroleum Geologist 63, pp. 2164–2182.

18. Dimech, A., Isabelle, A., Sylvain, K., Liu, C., Cheng, L., Bussière, B., Chouteau, M., Fabien-Ouellet, G., Bérubé, C., Wilkinson, P., Meldrum, P., and Chambers, J., 2023. A multiscale accuracy assessment of moisture content predictions using time-lapse electrical resistivity tomography in mine tailings. Scientific Reports 13:20922. https://doi.org/10.1038/s41598-023-48100-w

19. Dukhin S.S. and Shilov P., 1974. Dielectric Phenomena and the Double Layer in Disperse Systems and Polyelectrolytes. John Wiley & Sons, Inc., New York.

20. Evrard, M., Dumont, G., Hermans, T., Chouteau, M., Francis, O., Pirard, E., Nguyen, F., 2018. Geophysical Investigation of the Pb–Zn Deposit of Lontzen–Poppelsberg, Belgium. Minerals 8, 233 pp. https://doi.org/10.3390/min8060233.

21. Everett, M.E., 1997. Transient inductive coupiing of loops over near-surface clay-bearing sandstones. Society of Exploration Geophysicists 67th Ann. Internat. Mtg. (Dallas, TX, November 2-7).

22. Hayashi, M., 2004. Temperature-electrical conductivity relation of water for environmental monitoring and geophysical data inversion. Environment Monitoring Assessment 96, pp. 119–128.

23. Heenan, J., Porter, A., Ntarlagiannis, D., Young, L.Y., Werkema, D.D., Slater, L.D., 2013. Sensitivity of the spectral induced polarization method to microbial enhanced oil recovery processes. Geophysics 78 (5), E261–E269. http://dx.doi.org/10.1190/geo2013

24. Hermans, T., Nguyen, F., Robert, T., Revil, A., 2014. Geophysical methods for monitoring temperature changes in shallow low enthalpy geothermal systems. Energies 7, pp. 5083–5118.

25. Hermans, T., Wildemeersch, S., Jamin, P., Orban, P., Brouyère, S., Dassargues, A., Nguyen, F., 2015. Quantitative temperature monitoring of a heat tracing experiment using cross-borehole ERT. Geothermics 53, pp. 14–26.

26. Hermans, T., Irving, J., 2017. Facies discrimination with ERT using a probabilistic methodology: effect of sensitivity and regularization. Near Surface Geophysics 15, 13–25.

27. Hoang, P., 1997. Geological and Mineral Map of Phan Thiet, scale 1:50.000. Cent. Inf. Arch. J. Geol. C-49-37-A. Accessed on: http://idm.gov.vn/1P1NPIT/vi-VN/Ban-Do-Dia-Chat.aspx.(In Vietnamese). Accessed available: http://idm.gov.vn/1P1NPIT/vi-VN/Ban-Do-Dia-Chat.aspx. (In Vietnamese).

28. Hördt, A., et al., 2016. The dependence of induced polarization on fluid salinity and pH, studied with an extended model of membrane polarization. J. Applied Geophysics 135, pp. 408–417. http://dx.doi.org/10.1016/j.jappgeo.2016.02.007.

29. Hördt, A., Bairlein, K., Bücker, M., Stebner, H., 2017. Geometrical constraints for membrane polarization. Near Surface Geophysics 15 (6), pp. 579–592. https://doi.org/10. 3997/1873-0604.2017053.

30. Hort, Ryan D., Revil , André., Munakata-Marr, Junko., 2014. Analysis of sources of bulk conductivity change in saturated silica sand after unbuffered TCE oxidation by permanganate. Journal of Contaminant Hydrology, 165, pp 11-23. https://doi.org/10.1016/j.jconhyd.2014.07.003.

31. Huisman, J.A., Zimmermann, E., Esser, O., Haegel, F.-H., Treichel, A., Vereecken, H., 2016. Evaluation of a novel correction procedure to remove electrode impedance effects from broadband SIP measurements. Journal of Applied Geophysics. http://doi.org/10.1016/ j.jappgeo.2015.11.008.

32. Keller, G.V., Frischknecht, F.C., 1966. Electrical Methods in Geophysical Prospecting; Pergamon Press: Oxford, UK.

33. Kemna, A., Binley, A., Cassiani, G., Niederleithinger, E., Revil, A., Slater, L., Williams, K.H., Orozco1, A.F., Haege, F.H., Hördt, A., Kruschwitz, S., Leroux, V., Titov, K., and Zimmermann, E., 2012. An overview of the spectral induced polarization method for near-surface applications. Near Surface Geophysics 10, pp. 453-468. http://doi:10.3997/1873-0604.2012027.

34. Kemna, A., 2000. Tomographic Inversion of Complex Resistivity-Theory and Application. Ph.D. Thesis. Ruhr Universität, Bochum, Germany.

35. Ketabchi, Hamed., Sina Jahangir, Mohammad., 2021. Influence of aquifer heterogeneity on sea level rise-induced seawater intrusion: A probabilistic approach. Journal of Contaminant Hydrology, 236, 103753.

36. https://doi.org/10.1016/j.jconhyd.2020.103753

37. Klien, J. D., and Sill, W. R., 1982. Electrical properties of artificial claybearing sandstone: Geophysics 47, pp. 1593–1605.

38. Korošak, Dean., Cvikl, Bruno., Kramer, Janja., Jecl, Renata., Prapotnik, Anita., 2007. Fractional calculus applied to the analysis of spectral electrical conductivity of clay–water system. Journal of Contaminant Hydrology, 92, pp 1-9. https://doi.org/10.1016/j.jconhyd.2006.11.005.
39. Kremer, Thomas., Schmutz, Myriam., Leroy, Philippe., Agrinier, Pierre., Maineult, Alexis., 2016. Modelling the spectral induced polarization response of water-saturated sands in the intermediate frequency range (102–105 Hz) using mechanistic and empirical approaches. Geophysical Journal International, 207, 2, pp 1303–1312. https://doi.org/10.1093/gji/ggw334.
40. Krumbein, W.C., 1934. Size frequency distribution of sediments: Journal of Sedimentary Petrology 4,pp. 65-77.
41. Krumbein, W. C., and Sloss, L. L., 1963. Stratigraphy and sedimentation: 2nd ed., W. H. Freeman, San Francisco, 660 pp.
42. Leroy, P., Revil, A., Kemna, A., Cosenza, P., Ghorbani, A., 2008. Complex conductivity of water-saturated packs of glass beads. Journal of Colloid Interface Science 321 (1), pp. 103–117. https://doi.org/10.1016/j.jcis.2007.12.031.
43. Lyons, William C., 2010. Working guide to reservoir engineering. Published by Elsevier, first edition, pp.38.
44. Lesmes, D.P. and Morgan F.D., 2001. Dielectric spectroscopy of sedimentary rocks. Journal of Geophysical Research 106, pp. 13329–13346.
45. de Lima O.A.L. and Sharma M.M., 1992. A generalized Maxwell-Wagner theory for membrane polarization in shaly sands. Geophysics 57(3), pp. 431–440.
46. L. Insigne, M.S., and Kim, G.S., 2010. Saltwater Intrusion Modeling in the Aquifer Bounded by Manila Bay and Parañaque River, Philippines. Environmental Engineering Research 15 (2), pp. 117-121. http://doi.10.4491/eer.2010.15.2.117. pISSN 1225-1025 eISSN 2005-968X.
47. Loke, M.H., 2011. Tutorial: 2-D and 3-D Electrical Imaging Surveys.
48. Loke, M. H., Barker, R. D., 1996. Rapid least squares inversion of apparent resistivity pseudosections by a quasi-Newton method. Geophysical Prospecting 44, pp. 131-152.

49. Lowrie, W., 2007. Fundamentals of Geophysics, second edition. Assessed available: http://ebooks.cambridge.org/ebook.jsf?bid=CBO9780511807107.

50. McLachlan, P., Chambers, J., Uhlemann, S., Binley, A., 2020. Limitations and considerations for electrical resistivity and induced polarization imaging of riverbed sediments: Observations from laboratory, field, and synthetic experiments. Journal of Applied Geophysics, Vol 183, 104173. https://doi.org/10.1016/j.jappgeo.2020.104173.

51. Magnusson, M., Fernlund, J.R., Dahlin, T., 2010. Geoelectrical imaging in the interpretation of geological conditions affecting quarry operations. Bull. Engineering Geology Environment 69, pp. 465–486.

52. Martínez, J., Benavente, J., García-Aróstegui, J.L., Hidalgo, M.C., Rey, J., 2009. Contribution of electrical resistivity tomography to the study of detrital aquifers affected by seawater intrusion–extrusion effects: The river Vélez Delta (Vélez-Málaga, Southern Spain). Engineering Geology 108, pp. 161–168.

53. Marshall, D. J., and Madden, T. R., 1959. Induced polarization, a study of its causes: Geophysics 24, pp. 790–816.

54. McNeill, J.D., Bosnar, M., and Snelgrove, F.B., 1990. Resolution of an electromagnetic borehole conductivity logger for geotechnical and ground water applications: Geonics Technical Note TN–25, 28 pp.

55. Merriam J.B., 2007. Induced polarization and surface electrochemistry. Geophysics 72 (4), pp. 157-166.

56. Miall, A.D., 2000. Principles of Sedimentary Basin Analysis. Third, updated and enlarged edition. ISBN 978-3-642-08506-2. ISBN 978-3-662-03999-1 (eBook). https://doi 10.1007/978-3-662-03999-1.

57. Michael, HA., Scott, K.C., Koneshloo, M., Yu, X., Khan, M.R., Li, L., 2016. Geologic influence on groundwater salinity drives large seawater circulation through the continental shelf. Geophysical Research Letters 43, pp. 10782–10791. https://doi.org/10.1002/2016GL070863.

58. Moraa, Abrahan., Mahlknecht, Jürgen., Ledesma-Ruizb, Rogelio., E. Sanfordc., William., E. Lesser, Luis,. 2020.Dynamics of major and trace elements during seawater intrusion in a coastal sedimentary aquifer impacted by anthropogenic activities. Journal of Contaminant Hydrology, 232, pp 103653. https://doi.org/10.1016/j.jconhyd.2020.103653.
59. Motallebiana, Mahdi., Ahmadia, Hojjat., Raoof, Amir., Cartwright, Nick., 2019. An alternative approach to control saltwater intrusion in coastal aquifers using a freshwater surface recharge canal. Journal of Contaminant Hydrology, 222, pp.56-64. https://doi.org/10.1016/j.jconhyd.2019.02.007.
60. Najib, Saliha., Fadili, Ahmed., Mehdi, Khalid., Riss, Joëlle., Makan, Abdelhadi., 2017. Contribution of hydrochemical and geoelectrical approaches to investigate salinization process and seawater intrusion in the coastal aquifers of Chaouia, Morocco. Journal of Contaminant Hydrology, 198, pp.24-36. http://dx.doi.org/10.1016/j.jconhyd.2017.01.003.
61. Nasiri, Mina., Moghaddam, Hamid Kardan., Hamidi, Mehdi., 2021.. Development of Multi-Criteria Decision Making Methods for Reduction of Seawater Intrusion in Coastal Aquifers Using SEAWAT Code. Journal of Contaminant Hydrology, 242, 103848. https://doi.org/10.1016/j.jconhyd.2021.103848
62. Ntarlagiannis, D., Williams, K.H., Slater, L., Hubbard, S., 2005a. Low-frequency electrical response to microbial induced sulfide precipitation. Journal of Geophysical. Research 110. G02009. https://doi.org/10.1029/2005JG000024.
63. Nguyen, F., Kemna, A., Antonsson, A., Engesgaard, P., Kuras, O., Ogilvy, R., Gisbert, J., Jorreto, S., and Pulido-Bosch, A., 2009. Characterization of seawater intrusion using 2D electrical imaging. Near Surface Geophysics 7, No. 5–6: pp. 377–390.
64. Nguyen, T.T., Karl, S., Danie, U., Charles, N., Phung, V.P., Paul, L., DeMaster, D., Bui, V.D., Le, D.A., Mai, D.D., 2017. Surface sediment grain-sized distribution and sediment transport in the subaqueous Mekong Delta, Vietnam. Vietnam Journal of Earth Sciences 39(3), pp. 193-209, DOI: 10.15625/0866-7187/39/3/10266. Assessed available: https://vjs.ac.vn/index.php/jse/article/view/10266/pdf.

65. Nguyen Van Vuong., 1991. The quantitative lithological method for recognition of the unconsolidated sedimentary formation environments. Journals of geology, pp. 206 – 207. Assessed available: http://www.idm.gov.vn/nguon_luc/Xuat_ban/1991/a20611.htm.(In Vietnamese)
66. Ogilvy, A. A., and Kuzmina, E. N., 1972. Hydrogeologic and engineering-geologic possibilities for employing the method of induced potentials: Geophysics 37, pp. 839–861.
67. Olhoeft, G. R., 1985. Low-frequency electrical properties, Geophysics 50, pp. 2492–2503.
68. Post, V.E.A., M. Eichholz, R. Brentführer., 2018. Groundwater management in coastal zones. Bundesanstalt für Geowissenschaften und Rohstoffe (BGR). Hannover, Germany, 107 pp. Assessed available: https://www.bgr.bund.de/EN/Themen/Wasser/Produkte/Downloads/groundwater_management_in_coastal_zones.pdf?__blob=publicationFile&v=3.
69. Revil, A., Schmutz, M., Abdulsamad, F., Balde, A., Beck, C., Ghorbani, A., Hubbard, S.S., 2021. Field-scale estimation of soil properties from spectral induced polarization tomography. Geoderma, 403. https://doi.org/10.1016/j.geoderma.2021.115380.
70. Revil, A., Coperey A., Shao, Z., Florsch, N., Fabricius, I. L., Deng, Y., Delsman, J. R., Pauw, P. S., Karaoulis, M., De Louw, P. G. B., Van Baaren, E. S., Dabekaussen, W., Menkovic, A., and Gunnink, J. L ., 2017. Complex conductivity of soils, Water Resource Research 53, pp. 7121–7147, doi:10.1002/ 2017WR020655.
71. Revil, A., Florsch, N., and Camerlynck, C., 2014. Spectral induced polarization porosimetry. Geophys. J. Int. Vol. 198, 1016–1033, doi: 10.1093/gji/ggu180.
72. Revil, A., and M. Skold., 2011. Salinity dependence of spectral induced polarization in sands and sandstones, Geophysical Journal International 187, pp. 813–824, doi:10.1111/j.1365-246X.2011.05181. x.
73. Revil, A. & Florsch, N., 2010. Determination of permeability from spectral induced polarization data in granular media, Geophysical Journal International 181, pp. 1480–1498, doi:10.1111/j.1365-246X.2010.04573.x

74. Ronald L. Malcolm and V. C. Kennedy., 1970. Variation of Cation Exchange Capacity and Rate with Particle Size in Stream Sediment. Journal (Water Pollution Control Federation), Vol. 42, No. 5, Research Supplement to: 42, 5, Part II pp. 153-160. https://www.jstor.org/stable/25036587.

75. Rücker, C., Günther, T., Wagner, F.M., 2017. pyGIMLi: An open-source library for modelling and inversion in geophysics, Computers and Geosciences, 109, 106-123, doi: 10.1016/j.cageo.2017.07.011.

76. Saneiyan, S., Ntarlagiannis, D., Werkema, D.D., Ustra, A., 2018. Geophysical methods for monitoring soil stabilization processes. Journal of Applied Geophysics 148, pp. 234–244. https://doi.org/10.1016/j.jappgeo.2017.12.008.

77. Sara, J., Anders, L., Gianluca, F., and Dahlin, T., 2020. Spectral induced polarization of limestones: time domain field data, frequency domain laboratory data and physicochemical rock properties. Geophysical Journal International 220, pp. 928–950. https://doi: 10.1093/gji/ggz504.

78. Schön, J.H., 2011. Physical Properties of Rocks. Handbook of Petroleum Exploration and Production, vol. 8.

79. S. Colombano, H. Davarzani, E.D. van Hullebusch, D. Huguenot, D. Guyonnet, J. Deparis, I. Ignatiadis. 2019. Thermal and chemical-enhanced recovery of heavy chlorinated organic compounds in saturated porous media: 1D cell drainage-imbibition experiments. Science of the Total Environment 706, 135758. https://doi.org/10.1016/j.scitotenv.2019.135758.

80. Slater, L.D., Lesmes, D., 2002. IP interpretation in environmental investigations. Geophysics. 67, pp. 77–88.

81. Slater, L., Binley, A., Daily, W., Johnson, R., and Binley, A., 2000. Cross-hole electrical imaging of a controlled saline tracer injection: Journal of Applied Geophysics 44, pp. 85–102.

82. Szalai, S., Novák, A., Szarka, L., 2009. Depth of investigation and vertical resolution of surface geoelectric arrays. Journal of Environmental and Engineering Geophysics 14(1), pp.15–23. https://doi.org/10.2113/JEEG14.1.15.

83. Ta T.K.O., Nguyen V.L., Kobayashi I., Tateishi M and Saito Y., 2001. Late Pleistocene-Holocene stratigraphy and delta progradation, the Mekong River delta, South Vietnam. Gondwana Research 4(4), 779 pp. Assessed available: https://www.academia.edu/56550912/Late_Pleistocene_Holocene_Stratigraphy_and_Delta_Progradation_the_Mekong_River_Delta_South_Vietnam.

84. Tarasov, A., and Titov, K., 2007. Relaxation time distribution from time domain induced polarization measurements, Geophysical Journal International 170, pp. 31–43.

85. Tassy, A., Maxwell, M., Borgomano, J., Arfib, B., Fournier, F., Gilli, E., and Guglielmi, Y., 2014. Electrical resistivity tomography (ERT) of a coastal carbonate aquifer (Port-Miou, SE France). Environmental Earth Sciences 71, pp. 601–608. http://doi. 10.1007/s12665-013-2802-4.

86. Titov, K., Tarasov, A., Ilyin, Y., Seleznev, N., Boyd, A., 2010. Relationships between induced polarization relaxation time and hydraulic properties of sandstone. Geophysical Journal International 180, pp. 1095–1106. https://doi.org/10.1111/j.1365-246X.2009.04465.x.

87. Titov, K., Kemna, A., Tarasov, A., and Vereecken, H., 2004. Induced Polarization of Unsaturated Sands Determined through Time Domain Measurements. Vadose Zone Journal Vol 3, pp. 1160–1168.

88. Tran, N., Nguyen-Thanh, L., Dinh, X.T., Pham, N.H.V., Nguyen, H.S., Tran, T.T.N., 2007. Quaternary sedimentary cycles in relation to sea level change in Vietnam. VNU Journal of Science, Earth Sciences 23, pp. 235-243.

89. Vacquier, V., Holmes, R., Kintzinger, P. R., and Lavergne, M., 1957. Prospecting for ground water by induced electrical polarization: Geophysics 22, pp. 660–687.

90. Vandenbohede, A., Lebbe, L., Gysens, S. & De Wolf, P., 2008. Infiltration of salt water in artificial sea inlets in the Belgian dune area. In: Proceedings of the 1st SWIM-SWICA (19th Salt Intrusion Meeting – 3rd Salt Water Intrusion in Coastal Aquifers), pp. 239- 245.
91. Vaudelet, P., Revil, A., Schmutz, M., Franceschi, M. and Bégassat, P., 2011. Induced polarization signatures of cations exhibiting differential sorption behaviors in saturated sands. Water Resources Research 47(2), W02526, doi:10.1029/2010WR009310.
92. Vinegar, H.J. and Waxman, M.H., 1984. Induced Polarization of Shaly Sands. Geophysics 49, pp. 1267-1287. http://dx.doi.org/10.1190/1.1441755.
93. von Bülow, R., Klitzsch, N., and Wellmann, F., 2021. Strategies to overcome near surface disturbances while inverting time-lapse surface ERT data. Journal of Applied Geophysics 195,104463 pp. https://doi.org/10.1016/j.jappgeo.2021.104463.
94. Waxman, W.H., Smits L.J.M., 1968. Electrical conductivities in oil-bearing sands. Social Petroleum Engineering Journal 8, pp. 107-122.
95. Weigand, M., and Kemna, A., 2016. Relationship between Cole-Cole model parameters and spectral decomposition parameters derived from SIP data. Geophysical Journal International 205, pp. 1414–1419. https://doi: 10.1093/gji/ggw099.
96. Werner, Adrian D., Bakker , Mark,. Post, Vincent E.A,. Vandenbohede, Alexander., Lu, Chunhui., Ataie-Ashtiani, Behzad., Simmons, Craig T., Barry , D.A., 2013. Seawater intrusion processes, investigation and management: Recent advances and future challenges. Advance in Water Resources, 51, pp 3-26. https://doi.org/10.1016/j.advwatres.2012.03.004
97. Wentworth, C. K., 1922. A scale of grade and class terms for clastic sediments. Journal of Geology, vol. 30, 377 pp.
98. Winsauer, W.O., Shearin, H.M., Masson, P.H., Williams, M., 1952. Resistivity of brine-saturated sands in relation to pore geometry. AAPG Bull. 36, 253-277.
99. Zimmermann, E., Kemna, A., Berwix, J., Glaas, W., Münch, H.M., Huismann, J.A., 2008. A high-accuracy impedance spectrometer for measuring sediments with low polarizability. Measurement Science and Technology 19, 105603 pp. doi:10.1088/0957-0233/19/10/105603.

100. Zimmermann, E., Huisman, J.A., Kemna, A., Berwix, J., Glaas, W., Meier, H., Wolters, B., Esser, O., 2010. Advanced electrical impedance tomography system with high phase accuracy. Presented at the 6th World Congress on Industrial Process Tomography, pp. 583–591.

APPENDIX

A. SIP measurements (Zimmermann et al., 2008) and our cylinder-shaped sample holder.

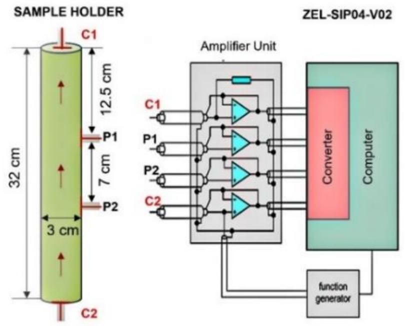

B. Graphs refer to phase shift spectra through the five salinity solutions in medium and fine sand categories are nearly flat at the low-frequency range.

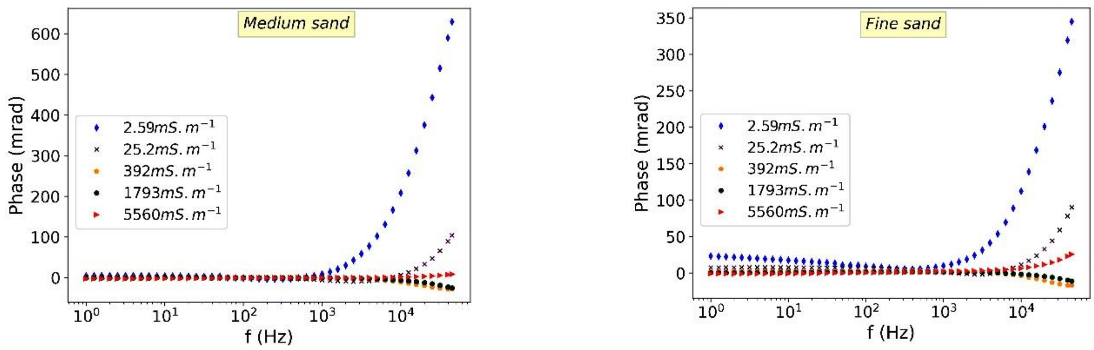

C. Total dissolved content (TDS) and electrical conductivity in the drilled boreholes of the Luy River Catchment in both dry and rainy seasons during two years.

Boreholes			**2020**		**2021**			
			Rainy season		**Dry season**		**Rainy season**	
No	**Name**	**Depth (m)**	**TDS (mg/L)**	**EC (mS/m at 25^{0}C)**	**TDS (mg/L)**	**EC (mS/m at 25^{0}C)**	**TDS (mg/L)**	**EC (mS/m at 25^{0}C)**
1	LK01-BT	32	11146	1715	43200	6646	6579	1012
2	LK02-BT	12	1664	256	1743	268	824	127
3	LK03-BT	17	8257	1270	11800	1816	6318	972
4	LK04-BT	8	941	145	2858	440	1251	193
5	LK07-BT	13.5	14212	2187	31620	4865	20610	3171
6	LK08*-BT	4.5	631	97	1315	203	471	73
7	LK09-BT	20.5	893	137	1435	221	694	107
8	LK10-BT	9	496	76	-	-	607	93

9	LK11-BT	13.5	512	79	570	88	303	47
10	LK12-BT	8	544	84	598	92	335	52
11	LK13-BT	23	880	135	1449	223	880	135
12	LK14-BT	16	1049	162	2010	309	1119	172
13	LK15-BT	13	535	82	362	56	132	20
14	LK16-BT	9	377	58	286	44	115	18
15	LK17-BT	21.5	2702	416	5645	869	1564	241
16	LK18-BT	13	579	89	1522	234	1540	237
17	LK19-BT	13.5	1277	197	1522	234	1102	170
18	LK20-BT	9	397	61	1184	183	139	21

953